UNIVERSITY OF TWENTE.

UMC Utrecht

Technical Medicine

Medical sensing and stimulation

Master Thesis

Naric Durmus

Development of a human peripheral myelinated axon model

Supervisors:

dr.ir. Boudewijn Sleutjes PDEng

dr. Hessel Franssen

Prof. dr. ir. Michel van Putten

Drs. Bregje Hessink-Sweep

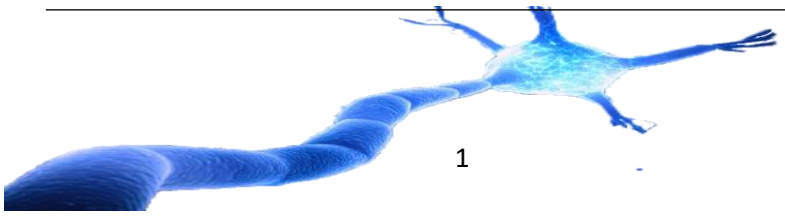

''Concision in style, precision in thought, decision in life.''
-Victor Hugo

PREFACE

Dear reader,

Before you lies my thesis, a one year research work at the neuromuscular group of UMC Utrecht. This thesis is written to fulfill the graduation requirements of Technical Medicine, Medical Sensing and Simulation at the University of Twente.

The past year was a great experience with ups and downs on the way. A lot of people helped me out to complete my thesis and motivated me whenever I lost interest.

First, I would like to thank my supervisors for their excellent guidance and support during this process. Special thanks to, Boudewijn Sleutjes, my technical supervisor at the hospital, who was with me at every step of the way in completing my thesis. He was always by my side and I could ask him anything. He was there to support me when I had harder times due to illnesses. I also want to thank Hessel Franssen, my medical supervisor, Maria Kovalchuk and Stephan Goedee, for their contribution at the medical field of my thesis. Not only was I busy with my research but had every opportunity to perform clinical duties with them. To my other colleagues at the department of Clinical Neurophysiology: I would like to thank you for the lovely workingplace they created and thanks for debating ideas about my research.

Furthermore, I want to thank Michel van Putten for his technical support from the University and Hil Meijer for reading my thesis and be a extern on the graduation committee. Special thanks to Bregje Hessink-Sweep, my process supervisor, who supported me to continue my work, gave me time to think about my growth as a technical physician and motivated me.

Lastly, I want to thank my parents for their motivations, my sisters for their insightful counsel, my brother and brothers in law for their support, my friends for being always kind and ready to help me out and my fiancée for being always by my side and believing in me.

I had fun writing, so I hope you will have fun reading!

Yours sincerely,

Nariç Durmus

Abstract

Introduction: Immune-mediated neuropathies are disorders affecting peripheral motor and sensory nerves, where nerve damage leads to loss of muscle power, loss of sensation, or both. The downstream mechanisms leading to the actual nerve dysfunction are not well understood and cannot be well-studied with the available experimental methods. Such as multifocal motor neuropathy(MMN), although peripheral nerve fascicles contain motor and sensory nerves, no sensory abnormalities are involved in MMN.

Methode: We developed a mathematical model of the human peripheral myelinated motor and sensory axon, which incorporates 41 successively connected nodes of Ranvier and detailed internodal regions including the paranode, juxtaparanode and standard internode with the myelin modelled using a double-cable structure, with a fiber diameter of 10.0 µm at 36 ^{o}C. To accurately simulate the human peripheral myelinated axon, we modified the parameters for the nodal and internodal membrane dynamics to those found in patch-clamp studies and used in human peripheral nerve excitability testing.

Main results. The sensory axon was simulated with respect to the motor axon by a decreased slow potassium channel conductance, an increased internodal inward rectifier current, a depolarizing shift of the voltage for half-activation for hyperpolarization-activated cyclic nucleotide–gated channels channels and depolarization of the resting membrane potential. Simulations with the developed models of a peripheral motor and sensory myelinated axon showed that the conduction velocities (CVs: motor: 47.3 m/sec, sensory: 50.6 m/sec) and strength-duration properties (motor: 204 µsec, sensory: 385 µsec) matched well with experimental studies. Further validation of the models was obtained by assessing the effects of temperature (36, 34, 32, 30, 28 and 26 ^{o}C), which showed an increase in CV with 1.52 m/sec/^{0}C for motor and 1.58 m/sec/^{0}C for sensory simulation, and an increase in fiber diameter (16 µm) shows an increase in CV of 79.5 m/sec for motor and 101.5 m/sec for sensory axons). All effects agreed with experimental data.

Significance. The developed model consists of detailed morphological and biophysical properties of the human peripheral myelinated motor and sensory axon. These computational platforms make it possible to systematically study downstream mechanisms of peripheral nerve diseases, which cannot be assessed with experimental studies. Obtaining insight into these mechanisms is essential, because it may provide knowledge on what morphological or functional elements are most likely targeted, which aids the development of novel treatment strategies to prevent irreversible nerve damage.

Keywords: mathematical model, peripheral myelinated axon, sensory axon, motor axon, neuropathies, multifocal motor neuropathy, demyelination, mechanical injuries

Abbreviations:

AMAN: Acute motor axonal neuropathy

CB: Conduction block

E_x: Nernst potential

F: Faradays constant [KC/mol]

GBS: Guillain–Barré syndrome

HCN-channels: Hyperpolarization-activated cyclic nucleotide–gated channels

IR: Inward rectifier

K_f: fast potassium

K_s: slow potassium

Lk: leakage

MMN: Multifocal motor neuropathy

Na: sodium

Na_p: persistent sodium

Na_t: transient sodium

Na/K pump: sodium/potassium pump

NCS: Nerve conduction study

R: Universal gas constant [MJ/K x mol]

SDTC: Strength-duration time constant

T: temperature [Kelvin]

Contents

1. Introduction

Human myelinated nerves in arms and legs have their primary function in transferring nerve impulses to mediate muscle movement or skin sensation. Immune-mediated neuropathies, such as Guillain–Barré syndrome (GBS), multifocal motor neuropathy (MMN) and acute motor axonal neuropathy (AMAN) are disorders where the body generates antibodies against its own nerves. As a result, they affect peripheral motor and sensory nerves, where nerve damage leads to loss of muscle power, loss of sensation, or both. Although the antibodies play a role in the initial attack against nerves, the downstream mechanism leading to the actual nerve dysfunction is not well understood. Knowledge of these mechanisms is essential for the development of treatments aimed at prevention of irreversible nerve damage.

Available methods in patients, like needle electromyography(EMG), EMG, nerve conduction studies (NCS), excitability test, single axon tracing, voltage or current clamp methods. These methods are invasive for the patient and are inaccurate, no channel disruptions or dynamics can directly be detected. These methods also take mostly a lot of time to perform(1,2). Furthermore, experimental methods in single myelinated axons are considerably more difficult to perform in mammalian and human fibers than in amphibian fibers, due to extreme fragility of the fibers and because they are surrounded by large connective tissue. Additionally, experimental findings in single myelinated amphibian or lower mammalian axons cannot always be extrapolated to human axons due to essential differences in ion-channel characteristics(3).

We developed a peripheral motor and sensory axon model with this present study and aimed to systematically study downstream mechanism, which cannot be assessed with experimental studies. For instance, about selective involvement of motor axons at the peripheral nerve level, such as in MMN and AMAN or about myelin damage that is associated with axonal conduction loss in trauma and chronic neurodegenerative diseases(4–6). With this peripheral axon simulation, patients do not have to come that often to a hospital for research purposes, clinical trials can be done more specific using outcome of the computer simulation. Computer simulations are relatively cheap and fast to perform, no additional tools are required.

Aim: The first step to develop a complex forward mathematical model of the human peripheral myelinated motor and sensory axon which incorporates all available functional knowledge on higher mammalian or human myelinated axons to study downstream mechanisms systematically in human neuropathies.

1.1 Normal physiology of a peripheral myelinated axon

A peripheral nerve consists of a bundle of motor and sensory axons. Each myelinated motor and sensory axon is surrounded by a myelin sheath, which is interrupted at the node of Ranvier(7,6). Myelination is a process whereby Schwann cells, elaborate double membrane wrappings around axons, creating an insulating layer that results in fast conduction of nerve impulses. The wrappings increase the total membrane resistance, decrease the total membrane capacitance and reduces the leakage of current between two adjacent nodes, which is essential for impulse propagation by saltatory conduction.(8) The speed of conduction between nodes of Ranvier depends on different aspects. The distance between the nodes of Ranvier is a determinant of the conduction velocity over the axons(9).

The node of Ranvier is in direct contact with the extracellular fluid, there is no myelin at the node of Ranvier. The axon area between adjacent nodes is called the internode, which is surrounded by Schwann cells (myelin). The internode consists of three main segments, the paranode, juxtaparanode and standard internode. The paranodal region is located adjacent to the node of Ranvier, where the myelin lamellae terminate in paranodal loops. Then follows the juxtaparanodal region, which has a very large surface area, because it has a fluted surface and the widest diameter, followed with the standard internode region(10,11).

The size of the internode varies and is positively correlated to the axon size. The node of Ranvier occupies approximately 0.1% of the total surface area of a node and internode together. The diameter of a myelinated axon ranges from 1-2 µm to 20 µm. The distance between two adjacent nodes is for the thickest fibers up to 1-2 mm. Thicker nerve fibers have a wider axon diameter, more myelin lamellae, a longer internodal distance and a faster internodal conduction velocity. The conduction velocity reaches a maximum in which conduction remains constant, despite longer internodes(9,10,12).

Adequate functioning of voltage-gated ion channels in nerve cells is essential for efficient signal transfer along the axons. Voltage-gated ion channels are specialized nerve cell membrane proteins. Voltage-gated ion-channels are not uniform distributed over the axolemma. Each channel is found in the above described axon segments, but the density per channel type differs between segments. The node of Ranvier contains mostly persistent and transient sodium(Na_t and Na_p) channels and slow potassium(K_s) channels. Fast potassium(K_f) channels have a very high density at the juxtaparanode(6). Hyperpolarization-activated cyclic nucleotide gated channel (HCN-channels) are located at the internode. As well as Na^+ channels and slow and K_f channels(6,13,14). The location of Na/K pumps are controversial, however advanced electrophysiological and immunostaining techniques suggest an internodal localization rather than nodal(15,16). A schematic overview of a myelinated axon can be seen in figure 1.

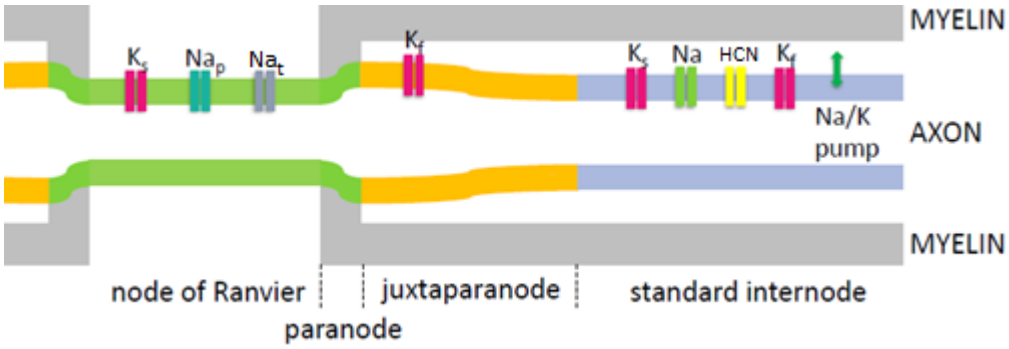

***Figure 1**: Myelinated axon diagram. Voltage-gated ion channels on the axolemma, which includes the node of Ranvier (light green), paranode(dark green), juxtaparanode(yellow), standard internode(blue). Channel descriptions; K_s: Slow potassium, Na_p: persistent sodium, Na_t: transient sodium, K_f: fast potassium, HCN: Hyperpolarization-activated cyclic nucleotide gated channels, Na/K pump: sodium/potassium pump.*

In the next chapter the development of the model will be explained. First a general description of the modal and then the motor model, continued by the differences of the sensory model and the ion channel specification. After the development procedure, the validation process will be explained and next an example of a clinical application will be given. The results will be discussed in the discussion and recommendation for further improvement will be made.

2. Model development

There are a lot of existing peripheral axon models(17–22), however, the model of McIntyre et al.(23) has also described paranodal, juxtaparanodal and internodal compartments in his model and was available in MATLAB and was easy to adjust to our needs. Therefore, we chose to extend the double cable model of McIntyre et al.(23) in this study.

2.1 General description of the model

The original model of McIntyre et al. (23) represents a detailed description of voltage-gated ion-channels in the node of Ranvier and simplified internodal membrane dynamics. As it does not contain internodal voltage-gated ion-channels, we extended the model by including a more detailed description of the internodal membrane dynamics and described the functional differences between peripheral human myelinated motor and sensory axon. As starting point, we used the MATLAB implementation of this model as published by Danner et al. (24), and subsequently modified it for the specific purposes of this study (MATLAB 2016b, MathWorks). Numerical integration of the differential equations was performed with the CVODE diferential equation solver from the Suite of nonlinear differential/algebraic equation solvers (SUNDIALS, version 2.6.1)(25) with time steps of 0.001ms. The sundialsTB MATLAB bindings, supplied with the SUNDIALS distribution were used to interface the CVODE solver in MATLAB.

For the longitudinal model we used in total 41 nodes of Ranvier separated by 40 internodes. The fiber geometry was kept as the original McIntyre et al.(23), where from node-to-node, the model consists of 11 segments geometrically representing the node(1 segment), paranode (paranodal myelin attachment, 1 segment), the juxtaparanode (paranodal main segment, 1 segment), the internode (6 segments), and again the juxtaparanode (1 segment), and paranode (1 segment), see figure 2 and 3.

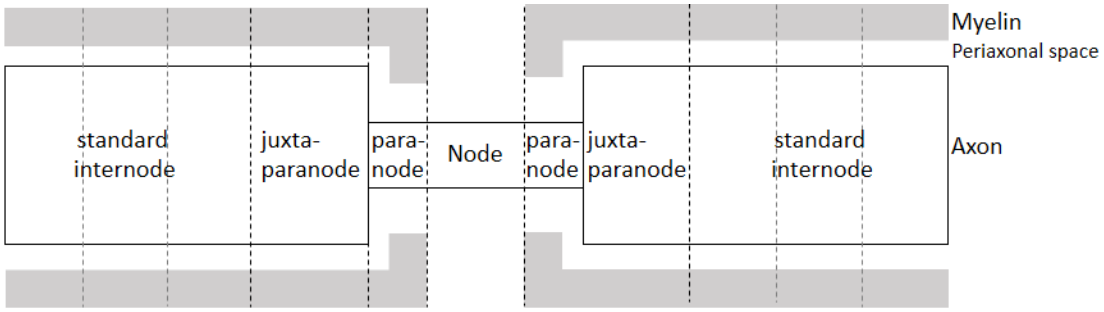

Figure 2: *Representation of the model with a node of Ranvier, a double cable structure with 2 paranodal segments, 2 juxtaparanodal segments and 6 standard internode segments in each compartment.*

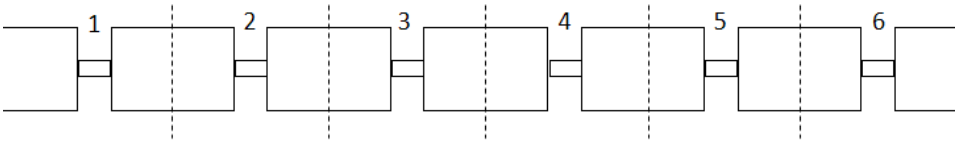

Figure 3*: Representation of the first 6 simulated components. With a total of 41 nodes of Ranviers and 40 internodal compartments.*

2.2 Nodal and internodal membrane dynamics of the myelinated motor axon model

We adjusted the original model as obtained by Danner et al.(24) which is based on the model of McIntyre et al.(23) and developed a peripheral motor and sensory axon simulation.

In the original model of McIntyre et al.(23) the node of Ranvier contained a voltage-gated Na_t and Na_p channels, voltage-gated K_s channels, a leak conductance and a nodal membrane capacitance. The dynamics of these ion-channels were based on experimental studies of Scholz et al.(26) Schwarz et al.(27) and Reid et al.(28) To simulate a human myelinated axon model as closely as possible, McIntyre et al. modified the parameters of membrane dynamics to those assessed in human peripheral motor nerve excitability test for fiber diameters of 10.0 µm, 14.0 µm and 16.0 µm, see table 1(19,20,23). Also, the temperature-dependency, and gating kinetics were based on earlier experimental work in human myelinated axons(23,26–28) . We chose to set the resting membrane potential at -80 mV in case of simulation of a peripheral motor axon.

The paranode was presented as a passive contributor by a conductance in parallel a capacitance at the axolemma(23). We chose not to implement channels in the paranode and kept it as the original. McIntyre et al.(23) described K_f channels in the juxtaparanode but chose not to use them in their study. Danner et al.(24) implemented an optional K_f channel in the juxtaparanode. Because K_f channels are certainly present in the juxtaparanode, we chose to implement them in our simulation(3,16,23). Furthermore, we implemented a non-specific leakage current to the juxtaparanode to compensate for channel isoforms or channels we did not incorporate in our study.

The original model of McIntyre et al.(23) did not describe any internodal channels. To more accurately describe the membrane dynamics in the internode, a series of ion-channels were additionally implemented. At the internode, the density of the Na channels has been suggested to be approximately 1/100 compared to that of nodal Na channels(3,13). Hence, internodal Na_t and Na_p channels were modelled by setting their conductance to 1% compared to that of the node. Based on Waxman et al.(16) also K_f and K_s channels are present in the internode. The estimated density of K_f channels in the internode compared to the juxtaparanode is about 1/6. For the K_s channels its density has been suggested to be 1/30 compared to that of the nodal density(14,16). Furthermore, the voltage-gated inwardly rectifying currents (IR) flow through, hyperpolarization-activated cyclic nucleotide gated channels (HCN-channels), and play an important role in pace-making, determination of the resting membrane potential, determination of axonal threshold in human motor axons and are also implemented in the internode. (20,29,30). Like the non-specific leakage current in the juxtaparanode, we implemented a current that may stand for the isoforms of channels we did not incorporate in our study (like the unmodeled slow HCN isoforms) (14). Finally, a Na^+/K^+-pump is implemented in the internode. Although, the localization of the Na^+/K^+-pump is controversial, it has been suggested to have an internodal localization(3,15,31). Therefore, a localization of the Na^+/K^+-pump in the internode is chosen, with a value of 0.1 nA(18,19,32).

An overview of the implemented ion-channels, the conductances and gating kinetics can be found in table 3. A schematic description of the mathematical model can be seen in figure 4, which represents the axolemma, and each compartments, with linear conductances in parallel with membrane capacitances. The electrical parameters of each compartment can be seen in table 2.

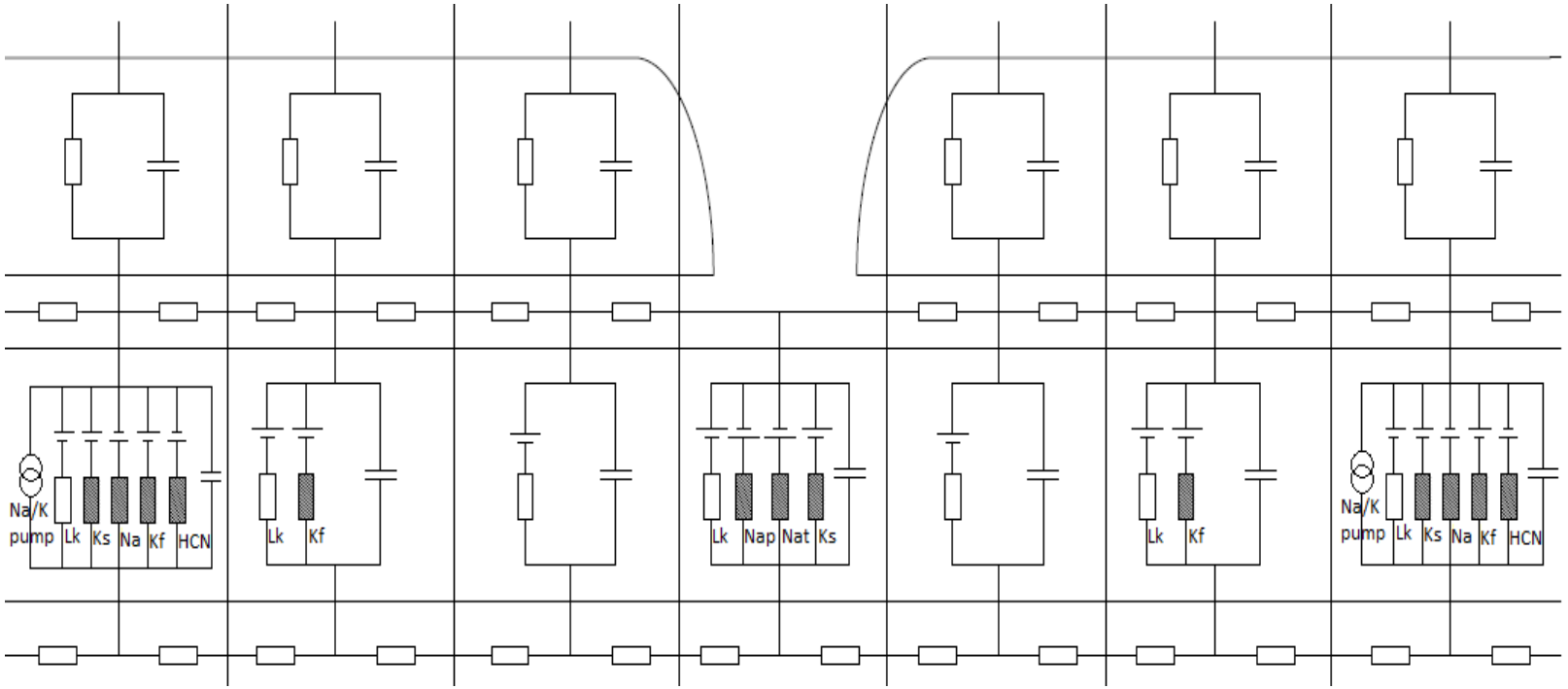

***Figure 4**: Schematic description of the mathematical model. The axon consists of the node of Ranvier, the paranode (myelin attachment region), juxtaparanodal region and standard internode region. The myelin and paranode both contains a linear conductance in parallel with the membrane capacitance. The juxtaparanodal region contains a parallel fast potassium channel (K_f) and a leakage(LK). The standard internodal region contains Na/K pump, leakage(LK), sodium(Na), HCN slow potassium(K_s) and fast potassium channel (K_f) channel parallel with each other. The node of Ranvier consists of a LK, persistent sodium(Na_p), transient sodium(Na_t) and K_s channel also parallel with each other.*

Table 1: *The model geometric parameters for fiber diameters of 10.0, 14.0 and 16.0 µm. Each compartment consists of 2 paranodal and 2 juxtaparanodal regions and 6 standard internodal regions. All parameters, beside the number of myelin lamella, are in µm.*

	Fiber diameter		
	10.0	14.0	16.0
Node-node separation(23,33)	1150	1400	1500
Number of myelin lamella(12,23)	120	140	150
Node length(23,34,35)	1	1	1
Node diameter(23,34,35)	3.3	4.7	5.5
Paranode length(11,23)	3	3	3
Paranode diameter(11,12,23)	3.3	4.7	5.5
Paranode periaxonal space width(11,23)	0.002	0.002	0.002
Juxtaparanode length(11,23)	46	56	60
Juxtaparanode diameter(11,12,23)	6.9	10.4	12.7
Juxtaparanode periaxonal space width(11,23)	0.004	0.004	0.004
Standard internode length(23,33)	175.2	213.5	228.8
Standard internode diameter(12,23)	6.9	10.4	12.7
Standard internode periaxonal space width(11,23)	0.004	0.004	0.004

Table 2*: Conductance and capacitance values of each compartment. The value in bracket is the value for sensory simulations if this is chosen different from the motor axon simulations.*

Vrest(23,36)	-80 mV (-78 mV)
Axoplasmic + periaxonal resistivity(23)	70 Ohm*cm
Myelin capacitance(23,37,38)	0.1 µF/cm^2
Capacitance of the nodal membrane[23,39]	2 µF/cm^2
Capacitance of the internodal membrane(23,39)	2 µF/cm^2
Myelin conductance(23)	0.001 S/cm^2
Paranodal conductance(23)	0.001 S/cm^2
Juxtaparanodal conductance(23)	0.0001 S/cm^2
Standard internodal conductance(23)	0.0001 S/cm^2
Na/K pump(18,32)	0.1 nA

The conductances values are all in S/cm^2, therefore, the conductances are automatically adjusted to differences in fiber diameters and other geometric differences. The conductances are converted into values in nS. The conductance in S/cm^2 is first converted to a conductance value in nS/µm^2. Then the formula: conductance in nS = conductance in nS/µm^2 x diameter x length x pi, is used. The capacity values are also recalculated to values of pF in the same manner. The same method is used with the channel conductances, these are given in table 3 for motor and sensory axons.

2.3 Nodal and internodal membrane dynamics of the myelinated sensory axon model

There are differences between motor and sensory axons. These are important to implement, so that a different model for sensory and motor axons can be used, to see the effects of peripheral nerve diseases, myelin damage and mechanical injuries on sensory and motor axons and for example answer questions about selective involvement of motor axons in MMN.

A prominent difference between sensory and motor axons has been suggested to be their accommodation to hyperpolarizing currents produced by HCN channels (40). The more significant accommodation to hyperpolarize currents have been ascribed to HCN channels, which are expressed more in sensory axons than in motor axons(20,31,40–43). Furthermore, increased expression of HCN channels has been suggested as a contributing factor to the greater anode break hyperexcitability seen in sensory axons(40,44). Therefore, we made adaptations to the HCN channels using the method of Howells et al. (20), combining an increase in the maximal conductance of HCN of 39% with a 13.1 mV depolarizing shift in Bq, the voltage activation of the conductance underlying HCN.

Experimental studies have shown that sensory axons are more depolarized than motor axons. Nodal and internodal slow potassium channels and the potassium equilibrium potential contribute to the resting membrane potential(14,31). Furthermore, it is hypothesized that reduces slow potassium channel expression contributed to increased susceptibility to ectopic activity in sensory axons(45,46). Adaptations to nodal slow potassium conductance is made based on the study of Howells et al. (20) and a of 49% is chosen in the sensory axon model(20). Whereas, we are using a fixed resting membrane potential in our model, adapting values of slow potassium will not eventually lead to depolarization. Therefore, the resting membrane potential of sensory axons more depolarized (-78 mV).

***Table 3**: Parameter and descriptions of the conductances of all the implemented channels in the model in S/cm^2.*

Parameter	Motor	Sensory	References
Maximum nodal Na_t^+ conductance (G_{NatN})	3.0	3.0	(16,23,26,27)
Maximum nodal Na_p^+ conductance (G_{NapN})	0.010	0.010	(23,47)
Maximum nodal K_s^+ conductance (G_{KsN})	0.080	0.0411	(20,23,26,27,48)
Nodal leakage conductance (G_{LkN})	0.007	0.007	(23)
Juxtaparanodal maximum K_f^+ conductance (G_{kf})	0.02	0.02	(23,48,49)
Internodal maximum Na^+ conductance	$G_{NafN}/100$	$G_{NafN}/100$	(3)
Internodal maximum K_s^+ conductance	$G_{KsN}/30$	$G_{KsN}/30$	(16,49)
Internodal maximum K_f^+ conductance	$G_{kf}/6$	$G_{kf}/6$	(16,49)
Internodal maximum HCN conductance	0.0016	0.0022	(18–20)
Internodal leakage conductance	$G_{LkN}/330$	$G_{LkN}/330$	(18,19)

2.4 Ion-channel specifications

Nernst potentials of Na^+, K^+ and HCN channels the model are calculated with the formula:

$$E_x = \frac{RT}{F} \log \frac{[K]o + Selx[Na]o - Selx[K]o}{[K]i + Selx[Na]i - Selx[K]i}$$

For the universal gas constant(R) 8315569.8 MJ / K x mol, temperature(T) 309 Kelvin, Faradays constant (F) 96485 KC/mol. The concentration Na^+ outside and inside are respectively 144.2 mol/m^3 and 9 mol/m^3. The concentration K^+ outside and inside are respectively 4.5 mol/m^3 and 155 mol/m^3. The selectivity of the channels are for Na^+ channels 0.9, for K^+ 0 and for HCN channels 0.097(20). The leakage reverse potential is set the same value as the resting membrane potential.

The voltage and time dependent parameters for the rate constants α and β can be found in table 4. The values between brackets are the different used for the sensory model. The values without brackets are the same for motor and sensory simulations. The difference between motor and sensory is a depolarizing shift of 13.1mV in α_q and β_q as described by Howells et al.(20).

Table 4: *Voltage and time dependent parameters for the rate constants, α and β for motor and sensory models, taken from McIntyre et al.(23) and Jankelowitz et al.(19). The values within the brackets are for the sensory model only.*

	A (m/s, at 309 K)	B (mV)	C (mV)
Fast potassium α_n	0.0462	83.2	1.1
Fast potassium β_n	0.0824	66	10.5
Transient sodium α_h	0.062	114	11
Transient sodium β_h	2.3	31.8	13.4
Transient sodium α_m	1.86	20.4	10.3
Transient sodium β_m	0.086	25.7	9.16
Persistent sodium channel α_{mp}	0.01	27	10.2
Persistent sodium channel β_{mp}	0.00025	34	10
Inward rectifier α_q	0.00057	103.1 (90)	13.7
Inward rectifier β_q	0.00057	103.1 (90)	13.7
Slow potassium α_s	0.00084	22.4	14.6
Slow potassium β_s	0.000509	90.1	13.49

The gating values of the different channels can be calculated with the following formula:

(1) $$\frac{dx}{dt} = [\alpha_x (1 - x) - \beta_x x] * q10^{[(Tac - Tref)/10]}$$

With x representing the different channels including, m,h, m_p , s, n, and q . The rate constants alpa and beta are given by:

(2) $$\alpha_m, \alpha_{mp}, \alpha_n, \alpha_s = ((A (V + B)) / (1 - e^{(-V-B)/C}))$$

(3) $$\beta_m, \beta_{mp}, \beta_n, \beta_s, \alpha_h = ((A (-V - B)) / (1 - e^{(V+B)/C}))$$

(4) $$\beta_h = A / (1 + e^{(-V-B)/C}))$$

(5) $$\alpha_q = A \cdot (e^{(-V-B)/C})$$

(6) $$\beta_q = A / (e^{(-V-B)/C})$$

The temperature dependence of the gating kinetics is expressed by q10. The rate of change equals q10 when the actual temperature (T_{ac}) increases with 10 degrees relative to the references temperature (T_{ref}). The q10 values for α_m, α_{mp}, β_m, β_{mp} are 2.2, for α_h, β_h is q10 2.9 and for α_n, α_s, α_q, β_n, β_s, β_q 3.0.

The currents of each channel are calculated with the following formulas:

(7) $$I_{na} = g_{na} \cdot m^3 \cdot h \cdot (V_m - E_{na})$$

(8) $$I_{nap} = g_{nap} \cdot p^3 \cdot (V_m - E_{na})$$

(9) $$I_{ks} = g_{ks} \cdot s \cdot (V_m - E_k)$$

(10) $$I_{kf} = g_{kf} \cdot n^4 \cdot (V_m - E_{na})$$

(11) $$I_{IR} = g_{IR} \cdot q \cdot (V_m - E_h)$$

(12) $$I_{Lk} = g_{Lk} \cdot (V_m - E_{Lk})$$

With V_m the membrane potential, E the Nernst potential of the channel and g the conductance of the channel, resulting in the current I.

After the development of the model it is validated using different methods. First of all the action potential dynamics are taken into account, secondly the gating kinetics and the currents induced by the channels. Next the effect of temperature and fiber diameter on the conduction velocity and action potential are studied and lastly some strength-duration properties are calculated. These are all explained in the following chapter.

3. Model validation

3.1 Methods

Simulations were conducted to generate the action potential, its propagation to measure the conduction velocity, the effect of temperature on conduction velocity and on the shape of the action potential, the effect of fiber diameter on the conduction velocity, and the strength-duration properties.

Single intracellular stimuli were delivered with a stimulus duration of 1 ms. The fiber diameter was set to 10.0 µm and the temperature to 36° C. To assess their effect on conduction velocity the fiber diameter was altered to 14.0 and 16.0 µm. By increasing the fiber diameter, also the axon diameter, node diameter, paranode and juxtaparanode and internode diameter increased. The length of the internode changed and the amount of lamella(myelin) surrounding the internode also increased, see table 1. The implemented temperature changes were adjusted with steps of 2 K from 299 K (26°C) till 309 K(36°C).

To calculate the conduction velocity, first, the derivative of the action potential was taken in every node from which the time points with maximum rising slope were determined. The internodal conduction velocity was then calculated by dividing the node-to-node distance (1150 µm, see Table 1) by the internodal conduction time. Averaging the internodal conduction velocities resulted in the overall conduction velocity of the model. To avoid boundary effects of the model the internodal conduction velocities and activation thresholds were derived from node 11 to 31.

To determine the activation threshold a binary search algorithm was applied as implemented by Hennings et al.(50) In the model, an action potential was defined as the myelinated axon was depolarized to 0 mV at the node.

From the action potential the maximum amplitude, rise time, fall time and total duration was determined. Rise and fall times were calculating by approximating the action potential as a triangle. The rise time was taken as the time from the intersection of the 10% of the difference between the resting membrane potential and the maximum amplitude till the moment of maximum amplitude. The falling time was calculated at the same manner using the falling edge (51,52).The total duration of the action potential was taken as the sum of the rise and falling times.

The strength-duration properties are characterized by the rheobase and the strength-duration time constant (SDTC)(53). SDTC is commonly assed in nerve excitability studies as a measure of axonal excitability where it depends on the biophysical properties of the axonal membrane at the node of Ranvier. It also provides information about Na channel functioning(54). Rheobase is defined as the theoretical asymptotic current required to just excite a nerve using a stimulus with infinite duration(3). For simulating the SDTC and rheobase the changes in activation threshold was determined by varying the stimulus duration from 1 ms to 0.2 ms in steps of 0.2 ms, which is similar to that of nerve excitability testing(54).

3.2 Action potential

In figure 5 the generated action potential at the middle node of the model (node 20) for the motor (blue) and sensory (red) axon is shown after applying a 1ms intercellular stimulus pulse at node 11 with a stimulus current of 1000nA. The sensory axon starts a little bit earlier with an action potential and has a slightly lower peak amplitude(motor: 24.4 mV, sensory: 23.5 mV). Compared with the motor action potential the sensory action potential is broader. The activation threshold of node 20 is 478 nA for the motor model and 294 nA for the sensory model. Following an action potential, the models generated the characteristic depolarizing(DAP, black arrouw) and hyperpolarizing afterpotentials(AHP, green arrow) (see Figure 8).

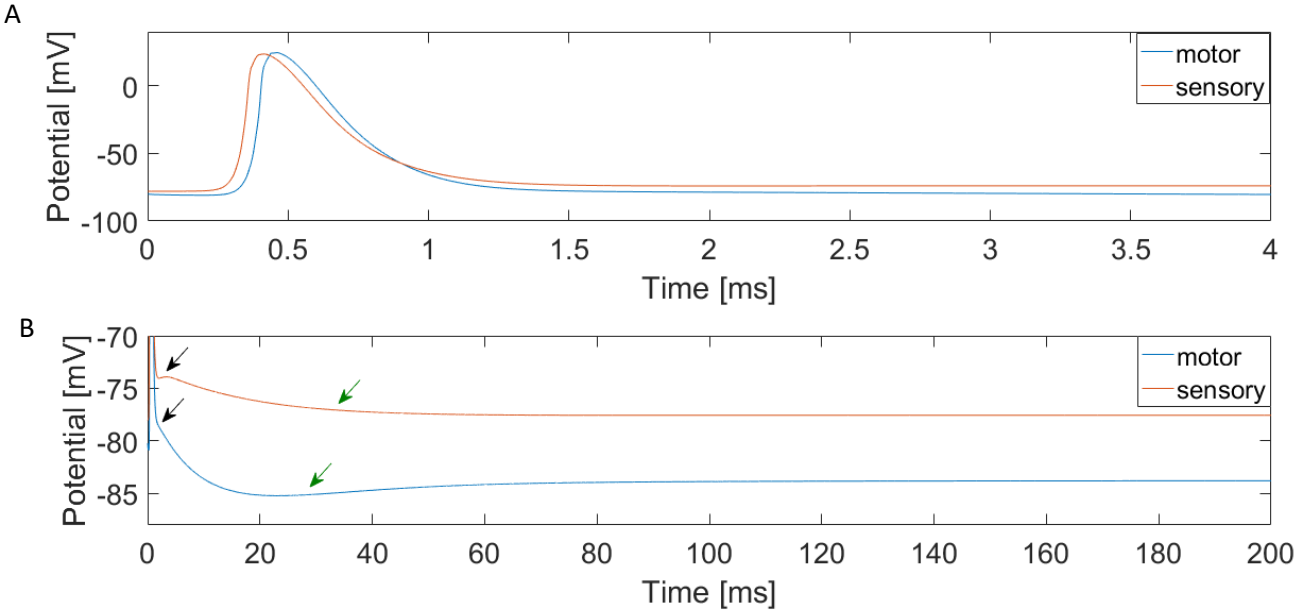

***Figure 5**: (A) The generated action potential of the motor (blue) and sensory (red) axon model up to 4ms from node 20. (B) Visualization of the same action potential as in (A), but close to its resting membrane potential(-80mV for motor and -78mV for sensory) from which the characteristic depolarizing after potential (DAP, black arrow) and hyperpolarizing afterpotential (AHP, green arrow) can be observed., for a duration of 200ms.*

3.3 Ion channel gating kinetics and currents

The validation of the model starts with observing the channel kinetics and currents. The mathematical model contains parallel ion channels. A correct implementation using Hodgkin-Huxley equations for the calculation of the channel currents and correct chosen voltage and time dependent parameters will show us channel gating kinetics varying between 0 and 1(55). Currents are defined by inward or outward currents, these are different in each ion channel.

Figure 6 shows the nodal gating kinetics and currents for motor (A) and sensory (B) axon simulations. No big differences between motor and sensory simulation could be observed. Figure 7 shows the nodal kinetics and currents for the K_f channel implemented in the juxtaparanode. The K_f channel current has a

higher peak in the sensory axon then in the motor simulation. Figure 8 shows the internodal gating kinetics and current values of the K_f and K_s, Na and HCN channels. The gating kinetics and currents are different in motor and sensory simulations.

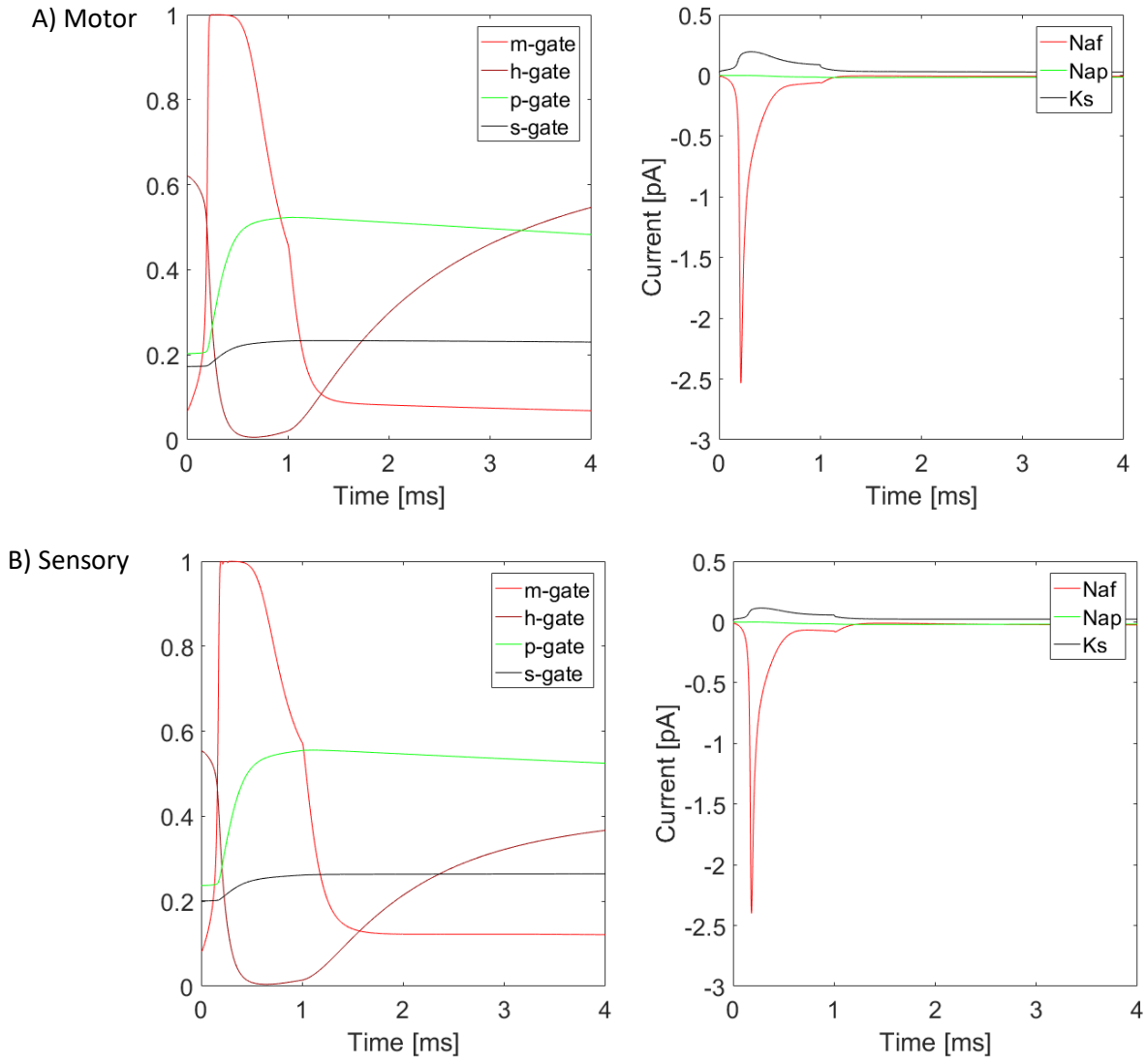

Figure 5: *The nodal gating kinetics for the implemented ion channels at node 20: transient(red) and persistent(green) sodium and slow potassium(black) channels. The gating kinetics are slightly different in motor (A) than in the sensory(B) simulation. Nodal current values of transient sodium (Na_t, red), persistent sodium(Na_p, green), slow potassium (Ks, black), are also shown at node 20. No big differences between motor(A) and sensory(B) simulations are seen.*

A) Motor

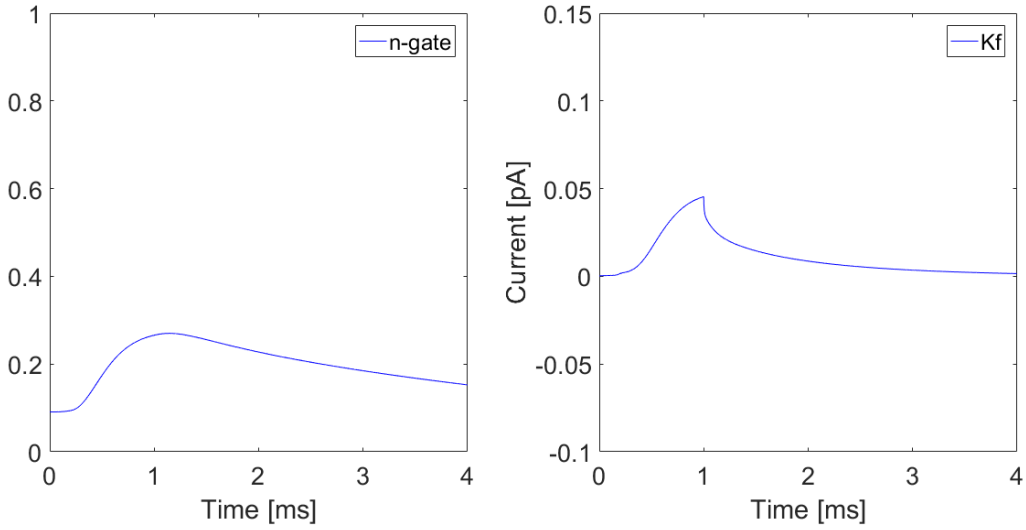

B) Sensory

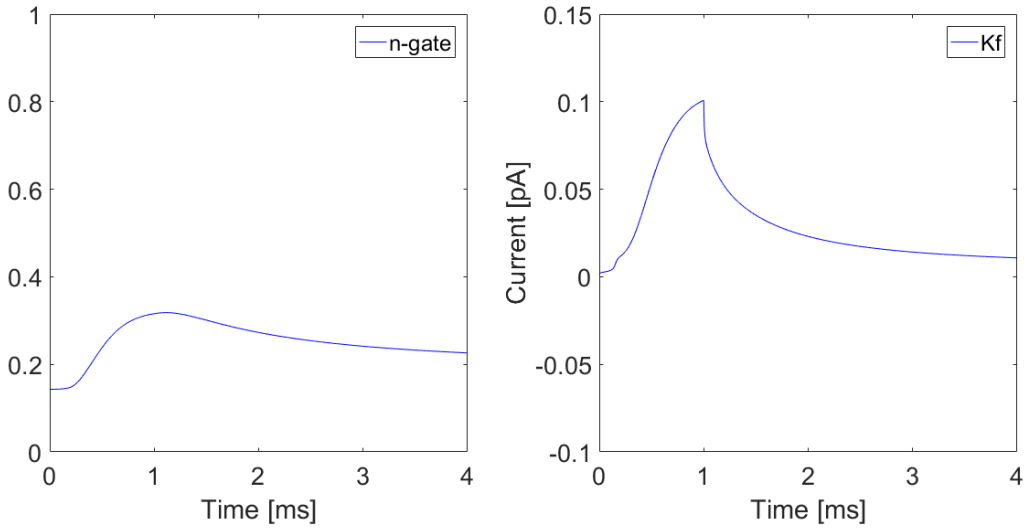

***Figure 7**: The gating kinetics of the fast potassium channel (n-gate) in the juxtaparanode at node 20. The n-gating kinetics are similar in motor (A) and sensory(B) simulations. Juxtaparanodal current values of fast potassium (Kf) at node 20. The juxtaparanode of the sensory(B) axon shows a higher peak current then the motor(A) model.*

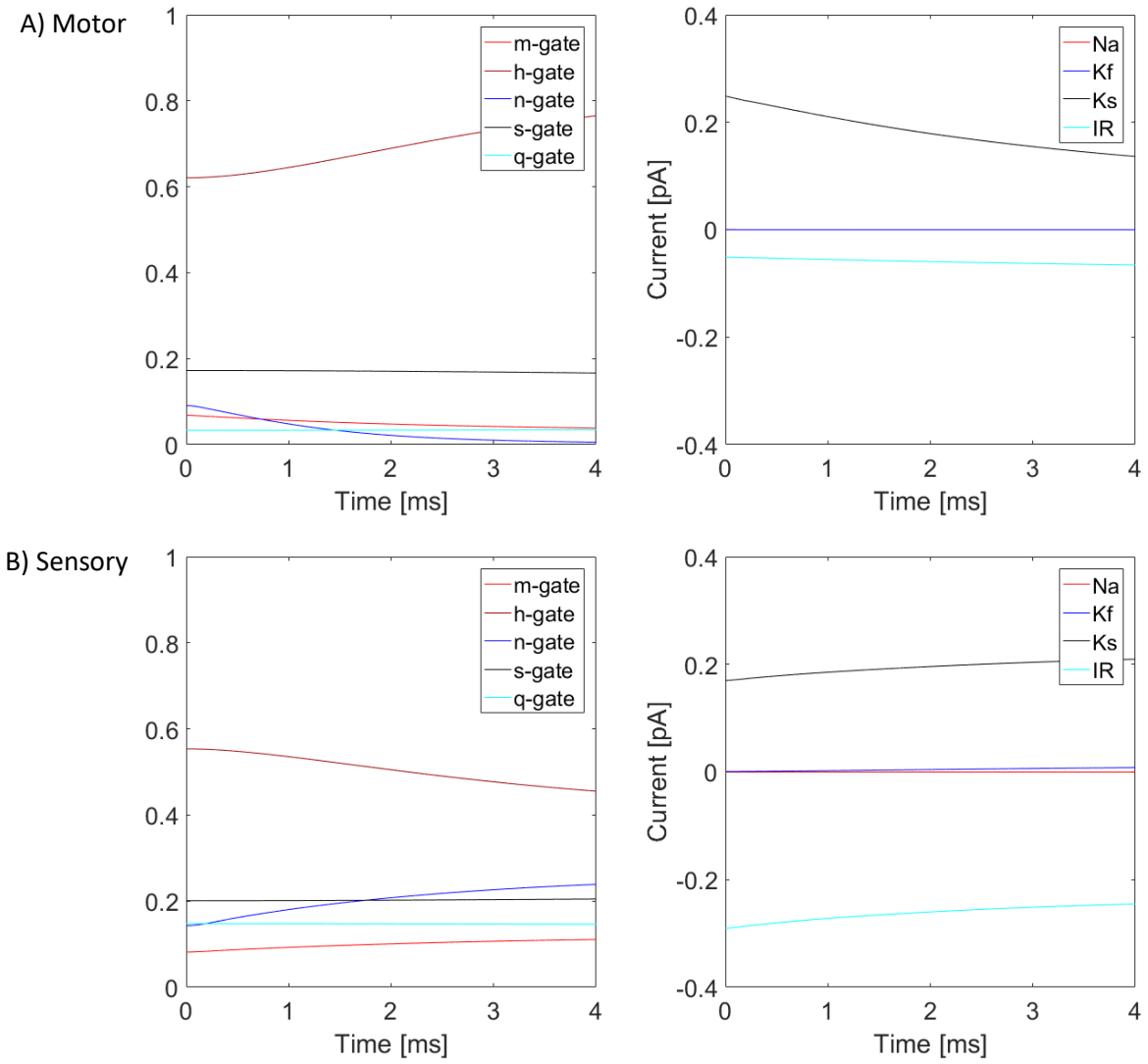

***Figure 8**: The gating kinetics of the fast potassium channel (n-gate), slow potassium (s-gate), sodium (m and h-gate) and HCN (q-gate) in the internode at node 20. Only the s-gate remains the same in motor(A) and sensory(B) axons. The remaining gating values are different in motor(A) and sensory(B) axons. Internodal current values for sodium (Na), fast potassium (Kf), slow potassium (Ks), Inward Rectifier current of the HCN channel (IR), leakage (Lk) and a total current value with all ion channels and leakage together at node 20. The form of the currents are different in motor (A) and sensory (B) axons.*

3.4 Fiber diameter.

The action potential propagation along nodes 11 to 31 for motor and sensory simulations can be seen in figure 9 A and B, where the line represents the steepest part from which the internodal conduction velocity was calculated, see section 3.1 for a detailed description on how the conduction velocity is calculated.

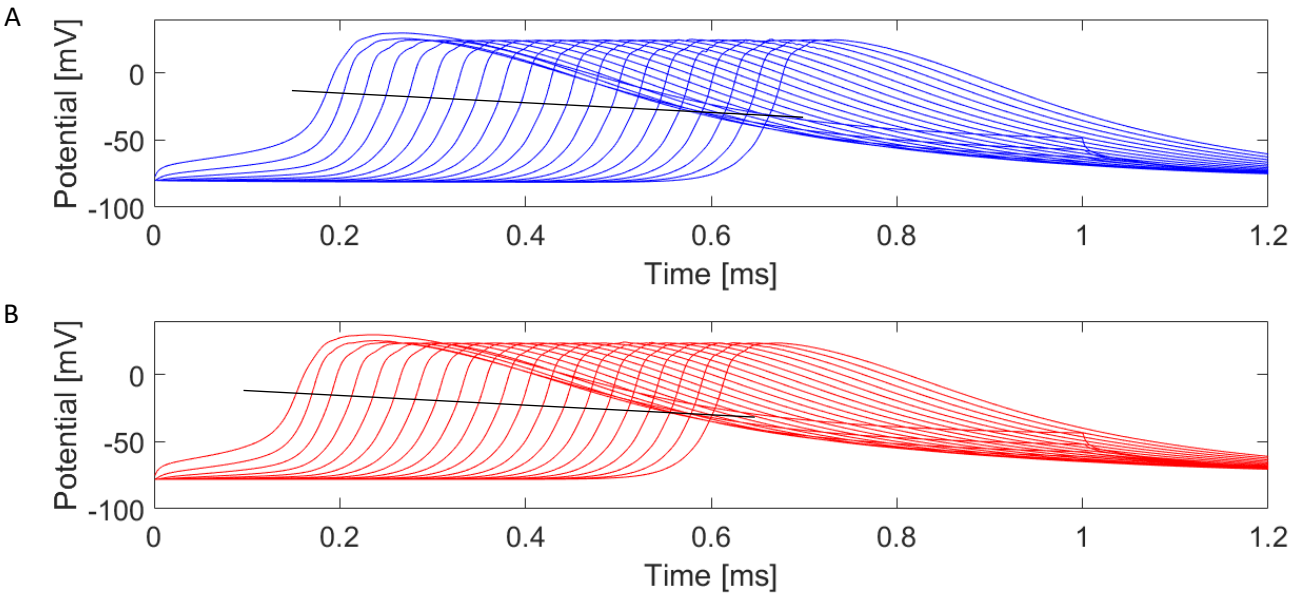

Figure 9: *Modeled action potentials at successive nodes of Ranvier(node number 11 till 31) in a model motor (A, blue) and sensory (B, red) myelinated axon. The black line represents the steepest points of the action potential*.

Changing the fiber diameter had an effect on the conduction velocity between motor and sensory axons. The conduction velocity for a fiber diameter of 10 µm was for motor and sensory axons respectively 49.9 m/sec and 53.4 m/sec. When the fiber diameter was increased to 14 µm and 16 µm the motor conduction velocity increased to respectively to 74.8 m/sec and 79.5 m/sec and the sensory conduction velocity to respectively 76.9 m/sec and 101.5 m/sec. The conduction velocity of the sensory axon is higher in respect to the conduction velocity of the motor axon and stays higher when the fiber diameter increases, see figure 10.

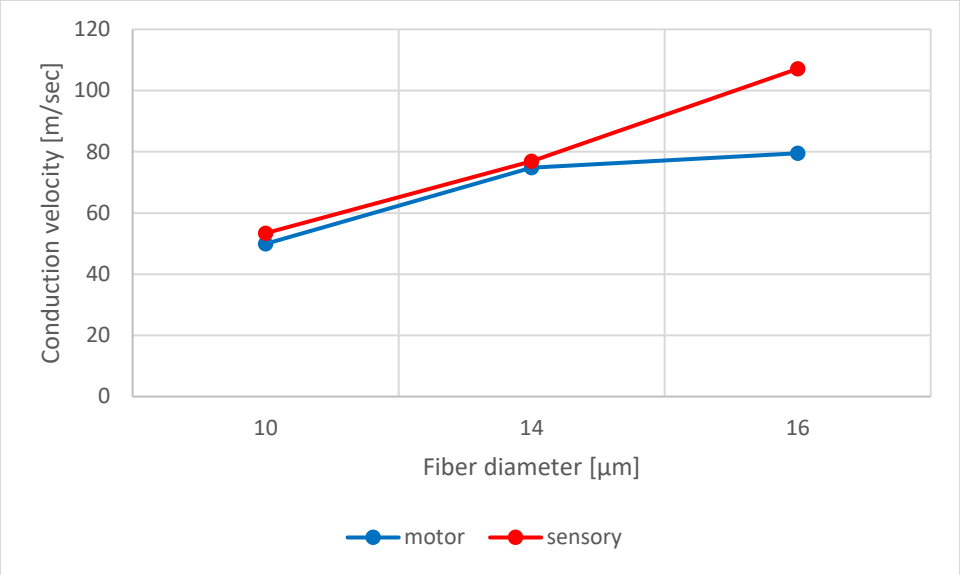

Figure 10: *Fiber diameter dependency of the conduction velocity for a motor (blue) and sensory (red) nerve fiber. The conduction velocity of the sensory axon remains higher than the motor axon and increases both when the fiber diameter increases.*

3.5 Temperature effects

In figure 11, the effect of temperature on the motor and sensory conduction velocity are shown with the expected increase in conduction velocity with increasing temperature in both the motor and sensory simulations.

The slope of the change in conduction velocity per degree in Celsius as calculated by taking a linear line from the conduction velocities 26 to 36°C and divide that with 10°C, was for the motor model 1.50 and the sensory model 1.51 m/s per °C The conduction velocity of motor axon simulations remained lower than the simulation of sensory axons. The q_{10} values as defined as a measure of the rate of change of because of the increasing temperature by 10 °C, are also different for motor and sensory simulations, which were respectively 1.44 and 1.40.

The action potential rise, fall and total times were calculated at temperatures of 26, 30 and 36°C. Figure 12 shows the definition of rise, fall and total times. Figure 13 shows the values of the rise and fall times for motor and sensory axons at different temperatures. Time rise, fall and total time decreased when the temperature increased in both motor and sensory simulations. The total action potential duration times are slightly more in sensory axon simulations in each chosen temperature, see figure 13. The maximum reached potentials of motor axons at a temperature of 26, 30 and 36°C were respectively 31.5 mV, 29.5 mV and 24.6. For sensory axons these were 30.9 mV, 28.9 mV and 23.6 mV.

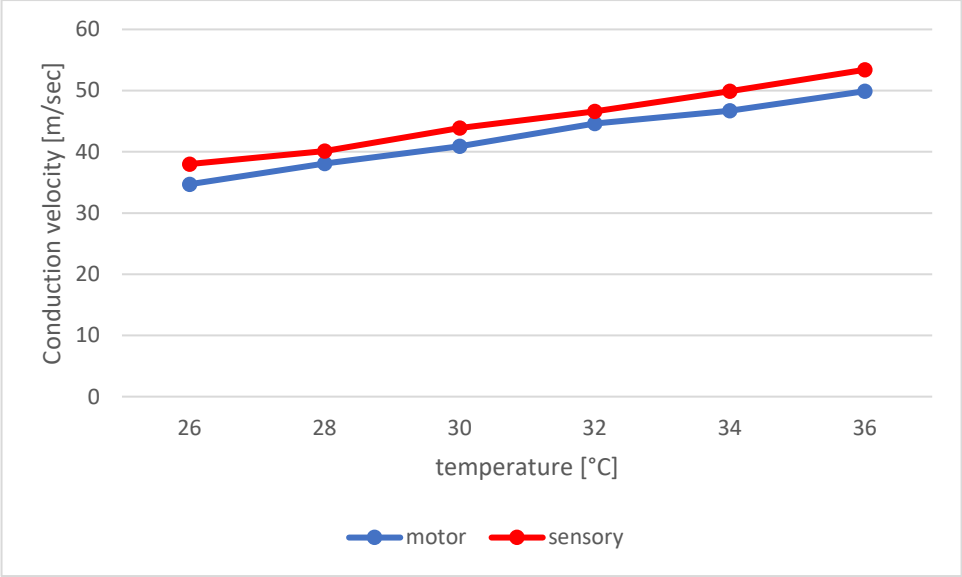

Figure 11: *Temperature dependency of conduction velocity for a motor and sensory nerve fiber. The conduction velocity of the sensory axon(red) remains higher than the motor axon(blue) and has a slightly higher slope value.*

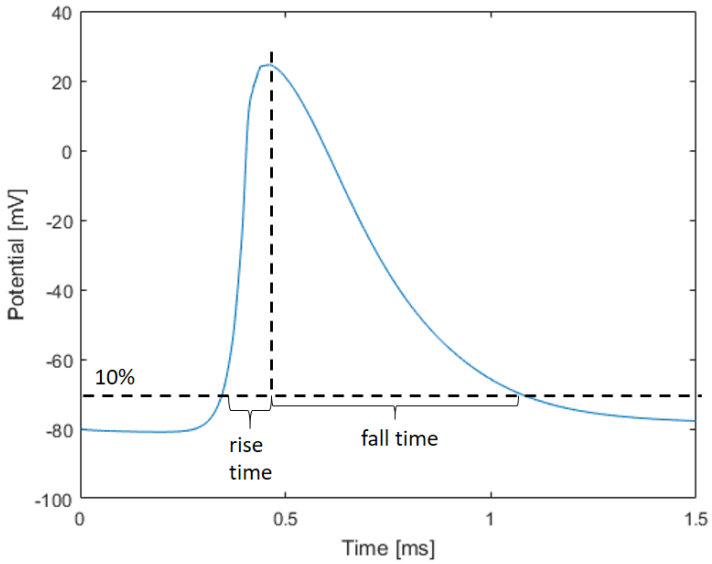

Figure 12: The description of the rise and fall time. The rise time starts at 10% of the action potential and continues till the maximum. The fall time starts at the maximum and ends at 10% of the action potential.

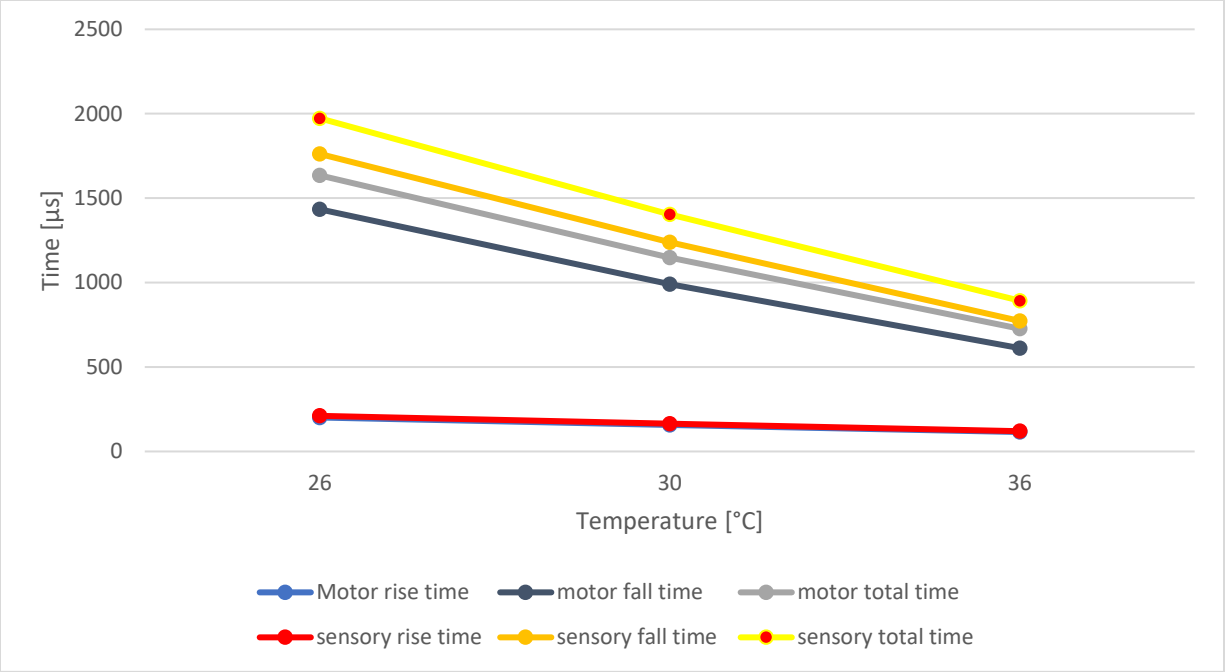

Table 13: *The rise, fall and total times of the action potentials for motor and sensory simulation at temperatures of 26°C, 30°C and 36°C. The sensory model simulation has a longer action potential duration at each chosen temperature.*

3.6 Strength-duration properties

The strength-duration properties were assessed by stimulating at node 21, using a transformation of Weiss's charge-duration equation, transformed as Bostock et al (53,56,57). Weiss proposed a linear equation using a charge Q duration curve. The electrical charge Q van be calculated with the formula:

(13) $$Q = I \cdot d \text{ or } Q = b(d + SDTC)$$

Where I is the current measured in amperes multiplied by the duration d. B relates to the rheobase value. Rheobase is the threshold current required if the stimulus is of infinitely long duration. In this formulation the SDTC equates to chronaxie (the stimulus duration corresponding to a threshold current that is twice rheobase). As can be seen, there is a linear relationship between charge and stimulus duration. Therefore, the rheobase and SDTC can be calculated from a charge-stimulus duration plot when different stimulus widths are used (see figure 14). The SDTC can be derived from the interception with the y-as (when the charge is 0), whereby the slope of this relationship corresponds to the rheobase.

The rheobase for the motor axon was higher with 393 pA compared to the sensory axon with 211 pA. The SDTC was lower for the motor axon with 204 µsec than the sensory axon with 385 µsec, see figure 14.

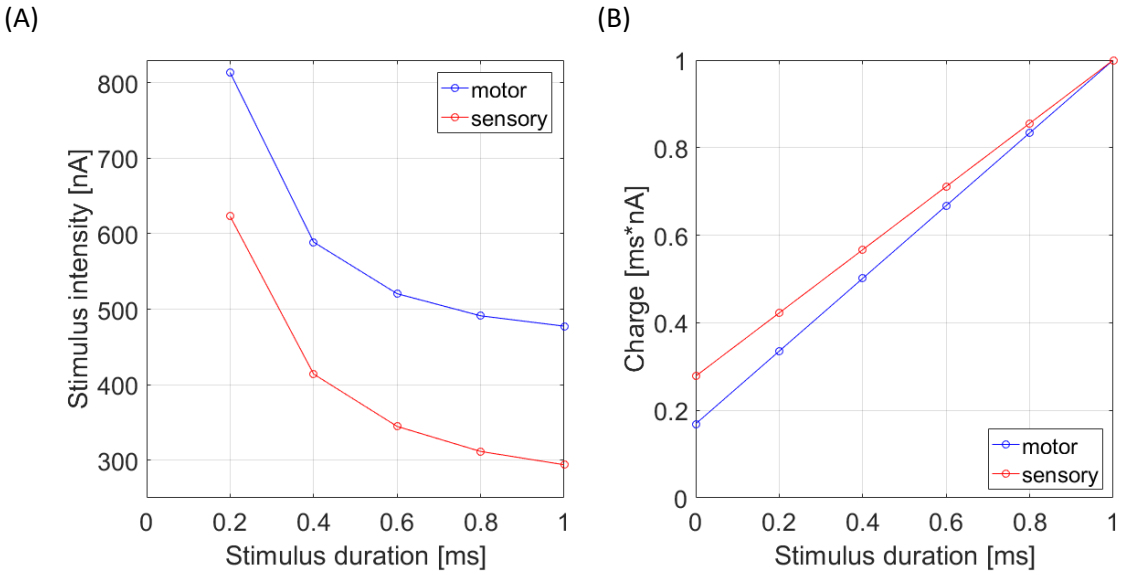

Figure 14: *(A) The strength duration curve for motor(blue) and sensory (red). The threshold value of the sensory model remains lower than the motor axon model. (B) The charge-duration curve for motor (blue) and sensory (red), the sensory charge remains larger than motor.*

4. Clinical application of the model

We gave to examples of clinical applications of the model in the introduction. First, we tried to answer questions about the selective involvement of motor axons in MMN.

4.1 Multifocal Motor Neuropathy

4.1.1 Introduction

Multifocal Motor Neuropathy(MMN) is characterized by progressive asymmetric weakness and atrophy of the muscles, due to focal conduction blocks(CB) along motor fibers. The presence of a CB in motor nerves, outside the usual sites of nerve compression, is an electrophysiological hallmark of MMN. A CB occurs when an action potential fails to propagate through a segment of an intact axon(58,59). Although, peripheral nerve fascicles contain motor as well as sensory axons, sensory symptoms are usually absent and sensory nerve conduction studies are often normal, also in segments with motor CB(1,2). The exact pathophysiological mechanism underlying CB is still unknown. Therefore, a computer simulation of the human peripheral myelinated axon which includes all available functional knowledge on higher mammalian or human myelinated motor and sensory axons is needed.

The most common theories about the developmont of CB in MMN are demyelination, a permanent altered resting membrane potential and nodal Na channel disruptions(2,60). Demyelination of an axon causes a reduced safety factor, which may lead to a CB. A safety factor is the ratio (available outward capacitative current = driving current)/(required inward ionic current = driving current) for the excitation of a node(3,61). There are different types of demyelination which can lead to a reduced safety factor, these are segmental demyelination, paranodal demyelination and juxtaparanodal demyelination. Segmental demyelination leads to a decreased driving current at the node that must be activated due to outward flowing of the driving current across the damaged myelin sheath, which eventually may result in a conduction block. Paranodal demyelination causes the driving current to be dissipated over an area consisting the node and the denuded paranode. The large capacitance of this area impairs depolarizaton of the former nodal area. Juxtaparanodal demyelination is similar to paranodal demyelination but depolarization is additionally impaired by activation of exposed juxtaparanodal K+ channels(3).

Intra and extra-cellular ion concentrations are important determinants for the resting membrane potential. The resting membrane potential is kept stable by maintaining the intracellular Na and K concentrations by active transport using Na/K pumps(62). Damage to voltage-gated Na-channels at the node will lead to loss of the action current and leads to a CB(6). Half of the MMN patients have anti-GM1 antibodies, suggesting an immune-mediated attack on nodal molecules(63–65). Anti-GM1 leads to structural alterations in paranodal regions and to subsequent disruption of the ion channel integrity, resulting in the formation of membrane attack complex, which allows uncontrolled ion influx due to compromises to the membrane integrity. Which eventually leads to disruption of Na channels(66). Experimental models also suggest that binding of anti-GM1 at the axolemma, causes blocking and disruption of Na channels associated with reduced nodal Na current density(3,67).

4.1.2 Simulation of MMN

Taken the information above into consideration three types of demyelination(segmental, paranodal and juxtaparanodal) could be simulated to have an overview of MMN. Furthermore, disruption of nodal Na channels could be added.

We first focused on modelling segmental demyelination. Segmental demyelination is when the whole part of the myelin, surrounding the paranode, juxtaparanode and internode are demyelinated, for a certain number of following internodes. Segmental demyelination is chosen for the comparison between motor and sensory axons because this type of demyelination leads to conduction block eventually(68). Focal segmental demyelination was simultaneously applied on the paranodal, juxtaparanodal, and internodal regions surrounding the three middle nodes(node 20, 21 and 22) by gradually increasing myelin capacitance and conductance, which corresponds with a certain percentage (30%, 50%, 70%, 95%, 96% and 97%) lamellae decrease, until conduction failure occurred.

Figure 15 and 16 show the propagation of the action potential of the motor(figure 15) and sensory(figure 16) axon after 50%, 96% and 97% demyelination. The potential decreases surrounding the demyelinated nodes but increases after the demyelinated area. Figure 15 shows that the motor axon reaches a state of conduction block after 96%. In case of the sensory axon this is at 97% demyelination.

Demyelination of the middle nodes causes a decrease of the conduction velocity resulting in conduction block eventually. The conduction velocity returns to normal after the signal passes the demyelinated nodes, as can be seen in figure 15 and 16.

Figure 17 shows a nice overview of the effect of demyelination on conduction velocity after a certain percentage demyelination. You can see that both in motor and sensory axons the conduction velocity decreases when the percentage demyelination increases.

The internodal conduction time is defined as the time of conduction between two adjacent nodes. The internodal capacitance increases when the percentage demyelination increases. Figure 18 shows the internodal conduction time over the internodal capacitance. Which shows an in general higher internodal conduction duration for motor axons and a steeper increase in the internodal conduction time for motor axons.

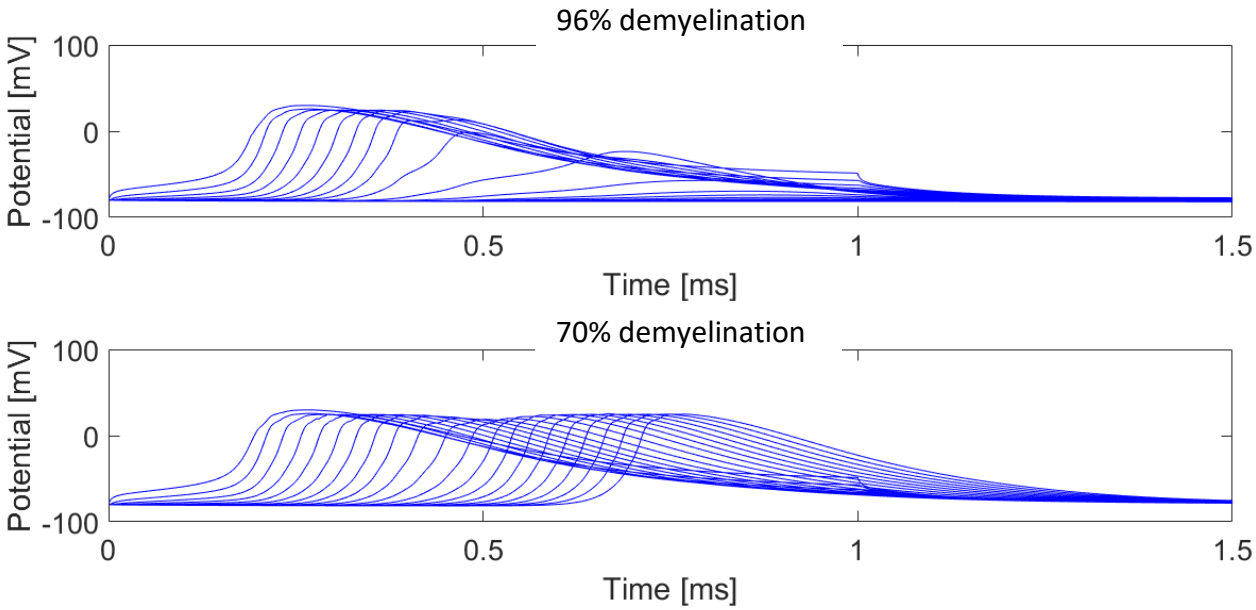

Figure 15: *The propagation of the action potential for 1.5 ms after 96% and 70% demyelination is shown for motor axon, resulting in a conducting block at 96% demyelination for the motor axon simulation and a decrease in the maximum potential at 70% in the middle nodes. The figures show the action potentials of node 11 till 31.*

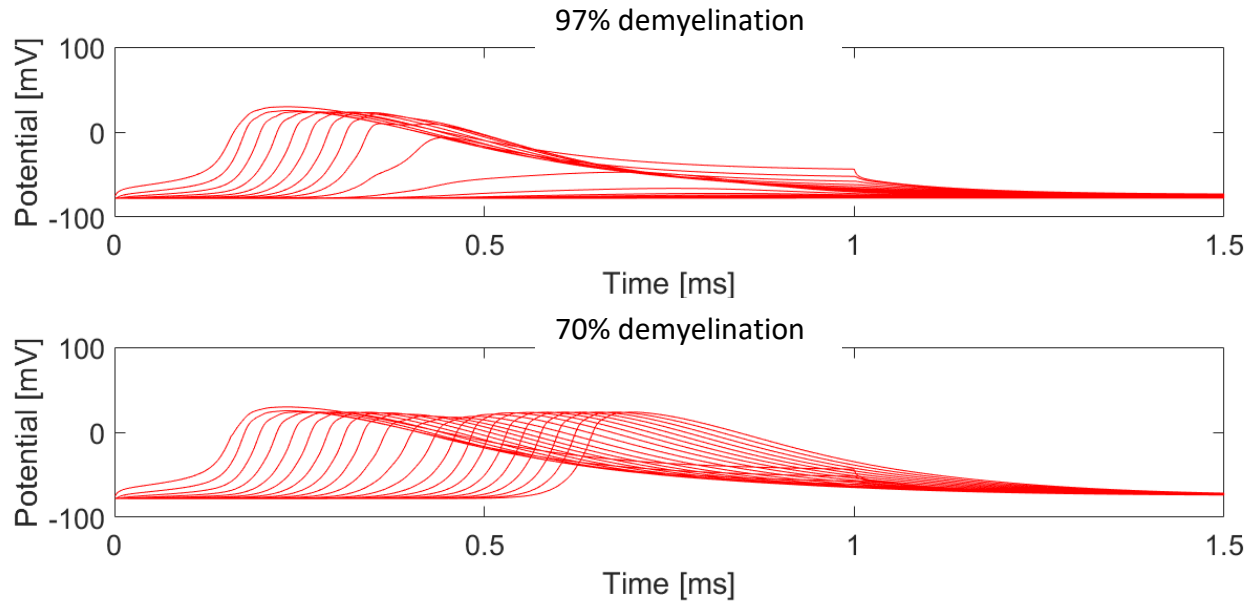

Figure 16: *The propagation of the action potential for 1.5 ms after 97% and 70% demyelination is shown for sensory axon, resulting in a conducting block at 97% demyelination for the sensory axon simulation and a decrease in the maximum potential at 70% in the middle nodes. The figures show the action potentials of node 11 till 31.*

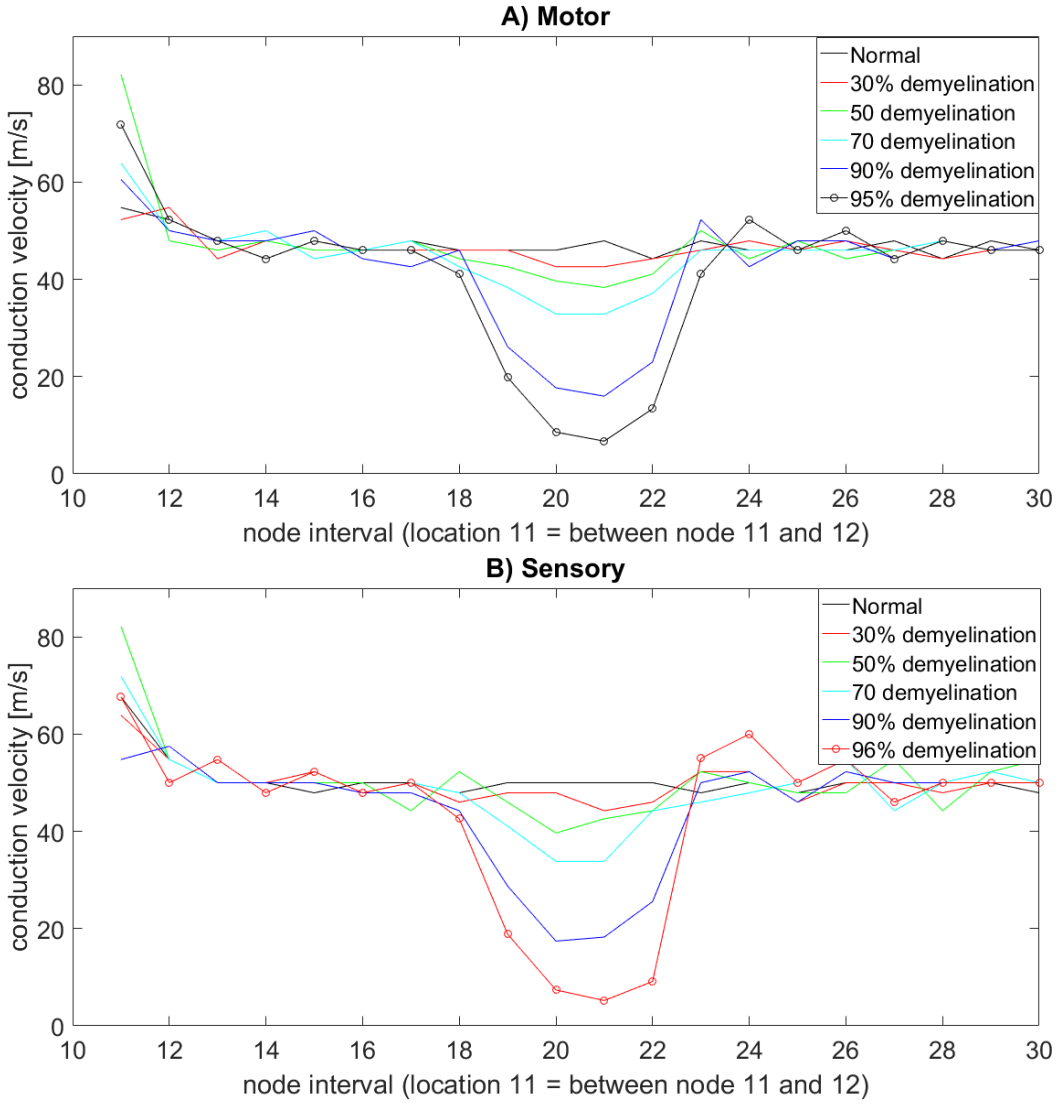

Figure 17: *Increasing the percentage demyelination decreases the conduction velocity for both motor (A) and sensory(B) model.*

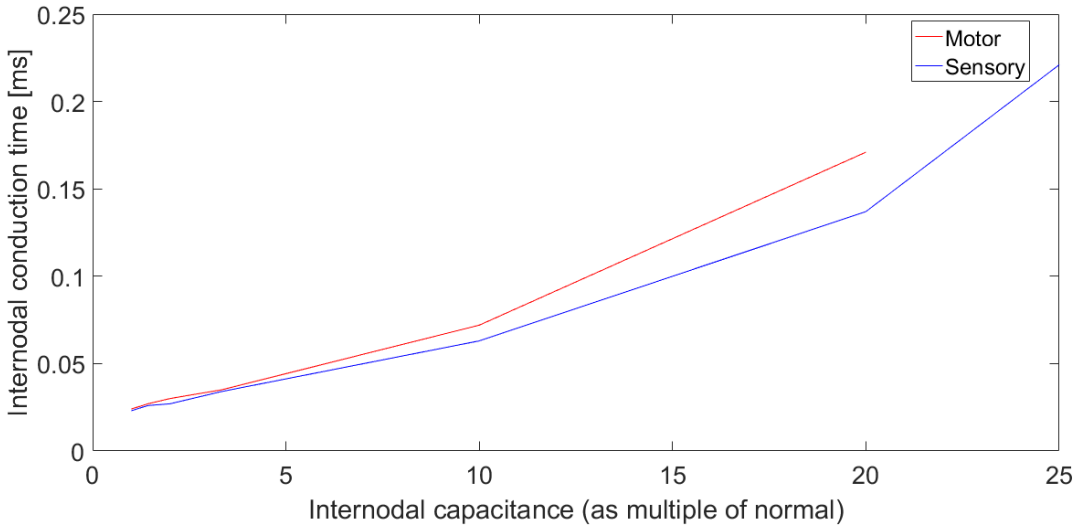

Figure 15: *Shows the internodal conduction duration over the internodal capacitance. The internodal conduction time is in general higher and steeper in motor(red) axons than in the sensory(blue) axon simulation*.

4.2 Example of future clinical application possibilities

Secure transmission of impulses along myelinated axons is essential for good conduction of the nerves. In various human neuropathies the clinical symptoms often indicate a prominent involvement of either motor or sensory axons. The immune-mediated neuropathy, MMN is a disorder where specifically peripheral motor nerves are affected with absence of sensory symptoms, while peripheral nerve fascicles contain both motor as well as sensory axons(1,6). The downstream mechanisms leading to the actual nerve dysfunction are not well understood and cannot be well-studied with the available experimental methods(1,2). One of the causes of conduction block in MMN is demyelination. The physiological consequences of demyelination of a single axon are slowing of the internodal conduction time, increased refractory period, persistent conduction block, rate-dependent block and warm block.(3) This can be validated after simulating demyelination. However, in the case of MMN, it remains unclear whether motor conduction block and slowing represent paranodal demyelination, segmental demyelination, changes in resting membrane potential or ion channel dysfunction at the node of Ranvier(2). To answer this question, segmental demyelination, paranodal demyelination, resting membrane deficit and an ion channel dysfunction may be implemented in the model.

Furthermore, the underlying mechanisms after mechanical injuries on peripheral nerves causing myelin disruption following axonal conduction failure could be studied and proper selection of drug treatment could be selected using treatment experiments. It is possible to simulate a mild and severe form of stretch or crush injury in the model. Using the definition of Babbs et al. (5) for a mild and severe form of stretch or crush injury. With a mild form of stretch or crush injury causing retraction of myelin around stretched nodes, which can be simulated by increasing the width of the exposed nodal membrane. A severe form of stretch or crush injury includes both retraction and detachment of paranodal myelin.

Which can be simulated by decreasing paranodal resistance to one tenth or one hundredth of its normal value(5).

The mathematical model can also be used in morphological question about peripheral nerves and a broader range of immune-mediated neuropathies. It is not limited to MMN or mechanical injuries.

As a result of the mathematical model being a good representation of experimental studies, it can also be used for education purposes, to understand ion-channel dynamics, the importance of morphological aspects in conduction, and action potential propagation.

5. Discussion

In this study, we developed and validated a longitudinal peripheral myelinated motor and sensory axon model with the aim to provide a platform to systematically study downstream mechanisms in human neuropathies. The computer simulation of McIntyre et al. (23) is adapted by including internodal channels to the model. Using knowledge about differences between peripheral motor and sensory axons, differences to the motor model are made to obtain a sensory axon model. The developed model is then validated by looking at the action potential of the models, check for the channel gating kinetics and currents, look at the fiber diameter dependency of the conduction velocity and the temperature dependency of the conduction velocity and action potential rise and fall times. The last validation step was to look at the SDTC and rheobase of the two models. The model is used in a clinical application, by showing the effect of segmental demyelination (for example with MMN), on the conduction velocity in motor and sensory axons, which resulted in an earlier conduction block in motor axons (at 96% demyelination) than sensory axons (at 97% demyelination). This platform further offers the opportunity to simulate effect of drugs when targeting at specific voltage-gated ion channels.

5.1 Development of the model.

In this study, we simulated peripheral myelinated motor and sensory axon action potential generation and propagation by applying single intracellular stimuli. With repetitive firing during e.g. voluntary activity, additional processes can occur, such as the increase in potassium concentration in the extracellular space, especially in the periaxonal space(23,69,70). This accumulation may play an important role when the axon fires at high frequencies for an extended period, because it influences the excitability of the axon(23,71,72). Although, this cannot be captured yet with the current model, the applied stimuli protocols resemble that of standard nerve conduction studies and nerve excitability studies.

Some studies suggest that a key difference between sensory and motor axons is also the greater expression of the Na_p channel current with 200%.(2) We did not change parameters of the Na_p channel to create a greater expression of the Na channel current. In our model we accounted the depolarization change for the need for a greater expression of Na_p current(14). In our model the Na_p current change is approximately 130%. Therefore, a change in percentage Na_p is not chosen.

The ion channel types, densities, and membrane dynamics of the mammalian node of Ranvier are not completely characterized. Therefore, our model included a representation, based on available experimental data. The ion channels were modified to reproduce several different experimentally documented excitation characteristics. Some of the ion channels therefore represent a combination of channels, which match best with experimental data, like potassium channels that are normally at least five different types(23,26–28,45,48).

5.2 Validation of the model

Validation of the motor and sensory axon models gave outcome which matched with experimental studies and other mathematical simulations. The action potential showed as expected a depolarizing and hyperpolarizing after potential(73). Conduction velocities were in range with experimental studies and nerve conduction studies (NCS) (74).

Differences between motor and sensory axons are also validated. Conduction velocities of the sensory axon remained higher in sensory axon simulations than motor axon simulations. A temperature increase, increased the conduction velocity in both motor and sensory axon, with a slightly higher slope in sensory axons as expected from previous conducted studies(44,75). The action potential was broader in sensory axons in respect to motor axons. This could be seen in the rise and fall time duration of both simulations(27,52,76,77). The broader action potential in sensory axons is earlier described and is suggested that the reduction of slow potassium channels at the node could be the reason(20). The temperature coefficient q_{10} was also within range of experimental studies(77). The conduction velocity increased with an increased axon diameter(78). Excitability studies have shown that motor axons have a smaller SDTC and larger rheobase than sensory axons(3,14,20,31,43,53,79,80). Also, a linear relationship between the charge and its duration is found as predicted by Weiss's formula(57).

5.3 Recommendations for further development of the model

No ion channels are implemented in the myelin, despite Schwann cells express several types of ion-channels. Different types of K^+ channels, Na^+ channels, Ca^{2+} channels and ligand-gated purinergic channels. Also, Na/K pumps are expressed in the Schwann cells(81,82). These channels can be important after repetitive firing, because these channel complexes may sustain rapid repolarization after an impulse and may prevent accumulation of potassium ions. However, we only used single spikes in this study, therefore we did not expect effect of potassium accumulation in our simulations, or the need of ion-channel implementation in the myelin.

We used ion channel conductances to use the Hodgkin-Huxley equation. Some mathematical models use permeability values(17–20,22). Using permeability values, and equations (see equation 14,15 and 16), gave us an unstable model, but the conductance values represented a good validation and where also earlier used by McIntyre et al. (23)

(14) $$I_{na} = P_{na} \cdot m^3 \cdot h \cdot z(Na)$$

(15) $$P_{na} \text{ in } cm^3/s \cdot 10^{-9}$$

(16) $$z = (EF^2 / RT) \cdot ([Na]_o - [Na]_i exp(EF / RT)) / (1-exp(EF/ RT)$$

For the validation of the model, the calculation of the conduction velocity was essential. The conduction velocity is calculated by taking the time of the steepest point of each action potential. The sample frequency of the model influences the precision of the calculation of this steepest point. The time difference between each adjacent node is taken and the node to node distance is divided by the passing time. The time that passes till the steepest point is also influenced by the sample frequency. Choosing a larger sample frequency results in an action potential signal simulation which takes time (10 minutes for a simulation of 5ms, with sample frequentie of 0.001ms). However, a decrease in simulation duration can be used to decrease the calculation time.

6. Conclusion

We successfully developed a longitudinal peripheral myelinated motor and sensory axon model which matches well with experimental studies. This platform provides a place to systematically study downstream mechanisms in human neuropathies. It offers for example to study selective involvement of motor axons in MMN and AMAN or the opportunity to simulate effect of drugs when targeting at specific voltage-gated ion channels. With this platform a direction can be given to clinical research and it can be performed more effectively.

7. References

1. Nowacek DG, Teener JW. Multifocal motor neuropathy. Semin Neurol [Internet]. 2012 Nov;32(5):500–5. Available from: http://www.ncbi.nlm.nih.gov/pubmed/23677657

2. Franssen H, Straver DCG. Pathophysiology of immune-mediated demyelinating neuropathies-Part II: Neurology. Muscle and Nerve [Internet]. 2014 Jan;49(1):4–20. Available from: http://doi.wiley.com/10.1002/mus.24068

3. Franssen H, Straver DCG. Pathophysiology of immune-mediated demyelinating neuropathies-part I: neuroscience. Muscle and Nerve. 2013;48(6):851–64.

4. Sun W, Fu Y, Shi Y, Cheng J-X, Cao P, Shi R. Paranodal myelin damage after acute stretch in Guinea pig spinal cord. J Neurotrauma [Internet]. 2012 Feb 10;29(3):611–9. Available from: http://www.ncbi.nlm.nih.gov/pubmed/21988176

5. Babbs CF, Shi R. Subtle Paranodal Injury Slows Impulse Conduction in a Mathematical Model of Myelinated Axons. Hamblin M, editor. PLoS One [Internet]. 2013 Jul 3;8(7):e67767. Available from: http://dx.plos.org/10.1371/journal.pone.0067767

6. Franssen H. The Node of Ranvier in Multifocal Motor Neuropathy. J Clin Immunol [Internet]. 2014 Jul 8;34(S1):105–11. Available from: http://link.springer.com/10.1007/s10875-014-0023-6

7. Swenson R. Review of clinical and functional neuroschience [Internet]. Dartmouth Medical School; 2006. Available from: https://www.dartmouth.edu/~rswenson/NeuroSci/index.html

8. Salzer JL. Schwann Cell Myelination. Cold Spring Harb Perspect Biol [Internet]. 2015 Aug;7(8):a020529. Available from: http://cshperspectives.cshlp.org/lookup/doi/10.1101/cshperspect.a020529

9. Wu LMN, Williams A, Delaney A, Sherman DL, Brophy PJ. Increasing internodal distance in myelinated nerves accelerates nerve conduction to a flat maximum. Curr Biol [Internet]. 2012 Oct 23;22(20):1957–61. Available from: http://www.ncbi.nlm.nih.gov/pubmed/23022068

10. Johnson C, Holmes WR, Brown A, Jung P. Minimizing the caliber of myelinated axons by means of nodal constrictions. J Neurophysiol [Internet]. 2015 Sep;114(3):1874–84. Available from: http://www.ncbi.nlm.nih.gov/pubmed/26224772

11. Berthold CH, Rydmark M. Electrophysiology and morphology of myelinated nerve fibers. VI. Anatomy of the paranode-node-paranode region in the cat. Experientia [Internet]. 1983 Sep 15;39(9):964–76. Available from: http://www.ncbi.nlm.nih.gov/pubmed/6884495

12. Berthold CH, Nilsson I, Rydmark M. Axon diameter and myelin sheath thickness in nerve fibres of

the ventral spinal root of the seventh lumbar nerve of the adult and developing cat. J Anat. 1983;136.

13. VOGEL W, SCHWARZ JR. Voltage-clamp studies in axons: Macroscopic and single-channel currents. In: The Axon [Internet]. Oxford University Press; 1995. p. 257–80. Available from: http://www.oxfordscholarship.com/view/10.1093/acprof:oso/9780195082937.001.0001/acprof-9780195082937-chapter-13

14. Burke D, Howells J, Kiernan MC. Sensory and motor axons are different: implications for neurological disease. Ann Clin Neurophysiol. 2017;19(1):3–12.

15. S. Kleinberg C, Arroyo E, King C, Scherer S. Na, K-ATPase isoforms in the PNS: Cell-type specific expression and internodal localization in myelinated axons. 2007. 45 p.

16. Waxman SG, Ritchie JM. Molecular dissection of the myelinated axon. Ann Neurol [Internet]. 1993 Feb;33(2):121–36. Available from: http://doi.wiley.com/10.1002/ana.410330202

17. Bostock H, Baker M, Grafe P, Reid G. Changes in excitability and accommodation of human motor axons following brief periods of ischaemia. J Physiol [Internet]. 1991;441. Available from: https://doi.org/10.1113/jphysiol.1991.sp018765

18. Stephanova DI, Bostock H. A distributed-parameter model of the myelinated human motor nerve fibre: temporal and spatial distribution sof action potentials and ionic currents. Biol Cybern. 1995;73:275–80.

19. Jankelowitz SK, Howells J, Burke D. Plasticity of inwardly rectifying conductances following a corticospinal lesion in human subjects. J Physiol [Internet]. 2007 Jun 15;581(3):927–40. Available from: http://doi.wiley.com/10.1113/jphysiol.2006.123661

20. Howells J, Trevillion L, Bostock H, Burke D. The voltage dependence of I(h) in human myelinated axons. J Physiol [Internet]. 2012 Apr 6;590(Pt 7):1625–40. Available from: http://www.ncbi.nlm.nih.gov/pmc/articles/PMC3413487/

21. Barrett EF, Barrett JN. Intracellular recording from vertebrate myelinated axons: mechanism of the depolarizing afterpotential. J Physiol [Internet]. 1982;323:117–44. Available from: http://www.ncbi.nlm.nih.gov/pmc/articles/PMC1250348/

22. Halter J, Clark J. A distributed-parameter model of the myelinated nerve fiber. J Theor Biol [Internet]. 1991;148. Available from: https://doi.org/10.1016/S0022-5193(05)80242-5

23. McIntyre CC, Richardson AG, Grill WM. Modeling the Excitability of Mammalian Nerve Fibers: Influence of Afterpotentials on the Recovery Cycle. J Neurophysiol [Internet]. 2002 Feb 1;87(2):995–1006. Available from: http://jn.physiology.org/lookup/doi/10.1152/jn.00353.2001

24. Danner S. Computer simulation of electrically stimulated nerve fibers in the human spinal cord. TU Wien; 2010.

25. Hindmarsh AC, Brown PN, Grant KE, Lee SL, Serban R, Shumaker DE, et al. SUNDIALS. ACM Trans Math Softw [Internet]. 2005 Sep 1;31(3):363–96. Available from: http://portal.acm.org/citation.cfm?doid=1089014.1089020

26. Scholz A, Reid G, Vogel W, Bostock H. Ion channels in human axons. J Neurophysiol. 1993;70.

27. Schwarz JR, Reid G, Bostock H. Action potentials and membrane currents in the human node of

Ranvier. Pflugers Arch [Internet]. 1995;430. Available from: https://doi.org/10.1007/BF00374660

28. Reid G, Scholz A, Bostock H, Vogel W. Human axons contain at least five types of voltage-dependent potassium channel. J Physiol [Internet]. 1999;518. Available from: https://doi.org/10.1111/j.1469-7793.1999.0681p.x

29. Pape H. Queer current and pacemaker: the hyperpolarization-activated cation current in neurons. Annu Rev Physiol [Internet]. 1996;58. Available from: https://doi.org/10.1146/annurev.ph.58.030196.001503

30. Biel M, Wahl-Schott C, Michalakis S, Zong X. Hyperpolarization-activated cation channels: from genes to function. Physiol Rev [Internet]. 2009 Jul;89(3):847–85. Available from: http://www.ncbi.nlm.nih.gov/pubmed/19584315

31. Burke D, Kiernan MC, Mogyoros I, Bostock H. Susceptibility to conduction block: differences in the biophysical properties of cutaneous afferents and motor axons. Physiolohy ALS Relat Dis. 1997;43–53.

32. Bostock H, Baker M, Reid G. Changes in excitability of human motor axons underlying post-ischaemic fasciculations: evidence for two stable states. J Physiol [Internet]. 1991;441. Available from: https://doi.org/10.1113/jphysiol.1991.sp018766

33. Nilsson I, Berthold CH. Axon classes and internodal growth in the ventral spinal root L7 of adult and developing cats. J Anat. 1988;156.

34. Rydmark M. Nodal axon diameter correlates linearly with internodal axon diameter in spinal roots of the cat. Neurosci Lett [Internet]. 1981;24. Available from: https://doi.org/10.1016/0304-3940(81)90165-8

35. Rydmark M, Berthold CH. Electron microscopic serial section analysis of nodes of Ranvier in lumbar spinal roots of the cat: a morphometric study of nodal compartments in fibres of different sizes. J Neurocytol [Internet]. 1983;12. Available from: https://doi.org/10.1007/BF01181523

36. Stys PK, Lehning E, Saubermann AJ, LoPachin RM. Intracellular concentrations of major ions in rat myelinated axons and glia: calculations based on electron probe X-ray microanalyses. J Neurochem [Internet]. 1997 May;68(5):1920–8. Available from: http://www.ncbi.nlm.nih.gov/pubmed/9109518

37. Tasaki I. New measurements of the capacity and the resistance of the myelin sheath and the nodal membrane of the isolated frog nerve fiber. Am J Physiol. 1955;181.

38. Huxley AF, Stämpfli R. Evidence for saltatory conduction in peripheral myelinated nerve fibres. J Physiol [Internet]. 1949 May 15;108(3):315–39. Available from: http://www.ncbi.nlm.nih.gov/pubmed/16991863

39. Bostock H, Sears TA. The internodal axon membrane: electrical excitability and continuous conduction in segmental demyelination. J Physiol [Internet]. 1978;280. Available from: https://doi.org/10.1113/jphysiol.1978.sp012384

40. Bostock H, Burke D, Hales J. Differences in behaviour of sensory and motor axons following release of ischaemia. Brain [Internet]. 1994;117. Available from: https://doi.org/10.1093/brain/117.2.225

41. Tomlinson S, Burke D, Hanna M, Koltzenburg M, Bostock H. In vivo assessment of HCN channel current (I h) in human motor axons. Muscle Nerve [Internet]. 2009;NA-NA. Available from: http://doi.wiley.com/10.1002/mus.21482

42. Howells J, Bostock H, Burke D. Accommodation to hyperpolarization of human axons assessed in the frequency domain. J Neurophysiol [Internet]. 2016 Aug;116(2):322–35. Available from: http://www.physiology.org/doi/10.1152/jn.00019.2016

43. Lin CS., Kuwabara S, Cappelen-Smith C, Burke D. Responses of human sensory and motor axons to the release of ischaemia and to hyperpolarizing current. J Physiol. 2002;541(3):1025–39.

44. Stephanova DI, Mileva K. Different effects of blocked potassium channels on action potentials, accommodation, adaptation and anode break excitation in human motor and sensory myelinated nerve fibres: computer simulations. Biol Cybern [Internet]. 2000;83(2):161–7. Available from: https://doi.org/10.1007/s004220000151

45. Baker M, Bostock H, Grafe P, Martius P. Function and distribution of three types of rectifying channel in rat spinal root myelinated axons. J Physiol. 1987;383.

46. Kocsis JD, Eng DL, Gordon TR, Waxman SG. Functional differences between 4-AP and TEA-sensitive potassium channels in mammalian axons. Neurosci Lett [Internet]. 1987;75. Available from: https://doi.org/10.1016/0304-3940(87)90296-5

47. Bostock H, Rothwell JC. Latent addition in motor and sensory fibres of human peripheral nerve. J Physiol. 1997;498(1):277–94.

48. Safronov B V, Kampe K, Vogel W. Single voltage-dependent potassium channels in rat peripheral nerve membrane. J Physiol [Internet]. 1993;460. Available from: https://doi.org/10.1113/jphysiol.1993.sp019493

49. Roper J, Schwarz JR. Heterogeneous distribution of fast and slow potassium channels in myelinated rat nerve fibres. J Physiol [Internet]. 1989;416. Available from: https://doi.org/10.1113/jphysiol.1989.sp017751

50. Hennings K, Arendt-Nielsen L, Andersen OK. Breakdown of accommodation in nerve: a possible role for persistent sodium current. Theor Biol Med Model [Internet]. 2005 Apr;2(1):16. Available from: https://doi.org/10.1186/1742-4682-2-16

51. Frijns JHM, Mooij J, ten Kate JH. A quantitative approach to modeling mammalian myelinated nerve fibers for electrical prosthesis design. IEEE Trans Biomed Eng [Internet]. 1994 Jun;41(6):556–66. Available from: http://ieeexplore.ieee.org/document/293243/

52. Smit JE, Hanekom T, Hanekom JJ. Modelled temperature-dependent excitability behaviour of a generalised human peripheral sensory nerve fibre. Biol Cybern [Internet]. 2009 Aug 5;101(2):115–30. Available from: http://link.springer.com/10.1007/s00422-009-0324-7

53. Mogyoros I, Kiernan MC, Burke D. Strength-duration properties of human peripheral nerve. Brain. 1996;119(2):439–47.

54. Burke D, Kiernan MC, Bostock H. Excitability of human axons. Clin Neurophysiol [Internet]. 2001 Sep;112(9):1575–85. Available from: http://www.ncbi.nlm.nih.gov/pubmed/11514239

55. Izhikevich EM. Dynamical Systems in Neuroscience: The Geometry of Excitability and Bursting.

London: The MIT Press Cambridge, Massachusetts; 2007. 2010 p.

56. Bostock H. The strength-duration relationship for excitation of myelinated nerve: computed dependence on membrane parameters. J Physiol [Internet]. 1983;341. Available from: https://doi.org/10.1113/jphysiol.1983.sp014792

57. Weiss G. Sur la possibility de rendre comparables entre eux les appareils servant a l'excitation electrique. Arch Ital Biol. 1901;35(1).

58. Ghosh A. A practical definition of conduction block in IvIg responsive multifocal motor neuropathy. J Neurol Neurosurg Psychiatry [Internet]. 2005 Sep 1;76(9):1264–8. Available from: http://jnnp.bmj.com/cgi/doi/10.1136/jnnp.2004.047688

59. Leger J-M, Guimaraes-Costa R, Iancu Ferfoglia R. The pathogenesis of multifocal motor neuropathy and an update on current management options. Ther Adv Neurol Disord [Internet]. 2015 May 1;8(3):109–22. Available from: http://tan.sagepub.com/cgi/doi/10.1177/1756285615575269

60. Nobile-Orazio E, Cappellari A, Priori A. Multifocal Motor Neuropathy: current concepts and controversies. Muscle and Nerve. 2005;31(6):663–80.

61. Kaji R, Sumner AJ. Ouabain reverses conduction disturbances in single demyelinated nerve fibers. Neurology. 1989;39(10):1364.

62. Straver DCG, van den Berg LH, van den Berg-Vos RM, Franssen H. Activity-dependent conduction block in multifocal motor neuropathy. Muscle and Nerve. 2011;43(1):31–6.

63. Vlam L, van der Pol W, Cats E, Straver D, Piepers S, Franssen H, et al. Multifocal motor neuropathy: diagnosis, pathogenesis and treatmen strategies. Nat Rev Neurol. 2011;8(1):48–58.

64. Santoro M, Uncini A, Corbo M, Staugaitis S, Thomas F, Hays A, et al. Experimental conduction block induced by serum from a patient with anti-GM1 antibodies. Ann Neurol. 1992;31(4):385–90.

65. Taylor B, Dyck P, Engelstad J, Gruener G, Grant I. Multifocal motor neuropathy: pathologic alterations at the site of conduction block. J Neuropathol Exp Neurol. 2004;63(2):129–37.

66. Harschnitz O, Jongbloed BA, Franssen H, Straver DCG, van der Pol WL, van den Berg LH. MMN: From Immunological Cross-Talk to Conduction Block. J Clin Immunol [Internet]. 2014 Apr 13;34(Suppl 1):112–9. Available from: http://www.ncbi.nlm.nih.gov/pmc/articles/PMC4050293/

67. Suzuki N, Kato S, Kato M, Warita H, Mizuno H, Kato M, et al. FUS/TLS-immunoreactive Neuronal and Glial Cell Inclusions Increase With Disease Duration in Familial Amyotrophic Lateral Sclerosis With an R521C FUS/TLS Mutation. J Neuropathol Exp Neurol [Internet]. 2012 Sep 1;71(9):779–88. Available from: http://dx.doi.org/10.1097/NEN.0b013e318264f164

68. Stephanova DI, Alexandrov AS, Kossev A, Christova L. Simulating focal demyelinating neuropathies: membrane property abnormalities. Biol Cybern [Internet]. 2007;96(2):195–208. Available from: https://doi.org/10.1007/s00422-006-0113-5

69. David G, Barrett JN, Barrett EF. Activation of internodal potassium conductance in rat myelinated axons. J Physiol [Internet]. 1993 Dec;472:177–202. Available from: http://www.ncbi.nlm.nih.gov/pubmed/8145140

70. Zhou L, Chiu SY. Computer model for action potential propagation through branch point in myelinated nerves. J Neurophysiol [Internet]. 2001 Jan;85(1):197–210. Available from: http://www.ncbi.nlm.nih.gov/pubmed/11152720

71. Bostock H, Bergmans J. Post-tetanic excitability changes and ectopic discharges in a human motor axon. Brain [Internet]. 1994 Oct;117 (Pt 5:913–28. Available from: http://www.ncbi.nlm.nih.gov/pubmed/7953601

72. Kapoor R, Smith KJ, Felts PA, Davies M. Internodal potassium currents can generate ectopic impulses in mammalian myelinated axons. Brain Res [Internet]. 1993 May 14;611(1):165–9. Available from: http://www.ncbi.nlm.nih.gov/pubmed/8518945

73. Blight AR, Someya S. Depolarizing afterpotentials in myelinated axons of mammalian spinal cord. Neuroscience [Internet]. 1985 May;15(1):1–12. Available from: http://linkinghub.elsevier.com/retrieve/pii/0306452285901186

74. Boyd IA, Kalu KU. Scaling factor relating conduction velocity and diameter for myelinated afferent nerve fibres in the cat hind limb. J Physiol [Internet]. 1979 Apr;289:277–97. Available from: http://www.ncbi.nlm.nih.gov/pubmed/458657

75. Dioszeghy P, Stålberg E. Changes in motor and sensory nerve conduction parameters with temperature in normal and diseased nerve. Electroencephalogr Clin Neurophysiol [Internet]. 1992 Aug;85(4):229–35. Available from: http://www.ncbi.nlm.nih.gov/pubmed/1380909

76. Wesselink WA, Holsheimer J, Boom HB. A model of the electrical behaviour of myelinated sensory nerve fibres based on human data. Med Biol Eng Comput [Internet]. 1999;37. Available from: https://doi.org/10.1007/BF02513291

77. Lowitzsch K, Hopf HC, Galland J. Changes of sensory conduction velocity and refractory periods with decreasing tissue temperature in man. J Neurol [Internet]. 1977 Oct 7;216(3):181–8. Available from: http://www.ncbi.nlm.nih.gov/pubmed/72136

78. Waxman SG. Determinants of conduction velocity in myelinated nerve fibers. Muscle Nerve [Internet]. 3(2):141–50. Available from: http://www.ncbi.nlm.nih.gov/pubmed/6245357

79. Kiernan MC, Burke D, Andersen K V, Bostock H. Multiple measures of axonal excitability: a new approach in clinical testing. Muscle Nerve [Internet]. 2000;23. Available from: https://doi.org/3.0.CO;2-G

80. Daskalova M, Stephanova DI. Strength-duration properties of human myelinated motor and sensory axons in normal case and in amyotrophic lateral sclerosis. Acta Physiol Pharmacol Bulg [Internet]. 2001;26(1–2):11–4. Available from: http://www.ncbi.nlm.nih.gov/pubmed/11693388

81. Mi H, Deerinck TJ, Ellisman MH, Schwarz TL. Differential distribution of closely related potassium channels in rat Schwann cells. J Neurosci [Internet]. 1995 May;15(5 Pt 2):3761–74. Available from: http://www.ncbi.nlm.nih.gov/pubmed/7751944

82. Baker MD. Electrophysiology of mammalian Schwann cells. Prog Biophys Mol Biol [Internet]. 78(2–3):83–103. Available from: http://www.ncbi.nlm.nih.gov/pubmed/12429109

Article: Developing a complex forward mathematical model of the human peripheral myelinated motor and sensory axon.

Nariç Durmus[1], Boudewijn T.H.M. Sleutjes[2], Maria O. Kovalchuk[2], Michel J.A.M. van Putten[3], Hessel Franssen[2]

[1]Biomedical Signals and Systems, MIRA, Institute for Technical Medicine and Biomedical Technology,[2]Department of Neurology and Neurosurgery, Brain Center Rudolf Magnus, University Medical Centre Utrecht, The Netherlands, and [3]Department of Clinical Neurophysiology, University Twente, Enschede, The Netherlands.

Abstract

Objective. Immune-mediated neuropathies are disorders affecting peripheral motor and sensory nerves, where nerve damage leads to loss of muscle power, loss of sensation, or both. The downstream mechanisms leading to the actual nerve dysfunction are not well understood and cannot be well-studied with the available experimental methods. Such as multifocal motor neuropathy(MMN), although peripheral nerve fascicles contain motor and sensory nerves, no sensory abnormalities are involved in MMN. *Approach.* We developed a mathematical model of the human peripheral myelinated motor and sensory axon, which incorporates 41 successively connected nodes of Ranvier and detailed internodal regions including the paranode, juxtaparanode and standard internode with the myelin modelled using a double-cable structure, with a fiber diameter of 10.0 µm at 36 °C. To accurately simulate the human peripheral myelinated axon, we modified the parameters for the nodal and internodal membrane dynamics to those found in patch-clamp studies and used in human peripheral nerve excitability testing. *Main results.* The sensory axon was simulated with respect to the motor axon by a decreased slow potassium channel conductance, an increased internodal inward rectifier current, a depolarizing shift of the voltage for half-activation for hyperpolarization-activated cyclic nucleotide–gated channels channels and depolarization of the resting membrane potential. Simulations with the developed models of a peripheral motor and sensory myelinated axon showed that the conduction velocities (CVs: motor: 47.3 m/sec, sensory: 50.6 m/sec) and strength-duration properties (motor: 204 µsec, sensory: 385 µsec) matched well with experimental studies. Further validation of the models was obtained by assessing the effects of temperature (36, 34, 32, 30, 28 and 26 °C), which showed an increase in CV with 1.52 m/sec/^{0}C for motor and 1.58 m/sec/^{0}C for sensory simulation, and an increase in fiber diameter (16 µm) shows an increase in CV of 79.5 m/sec for motor and 101.5 m/sec for sensory axons). All effects agreed with experimental data. *Significance.* The developed model consists of detailed morphological and biophysical properties of the human peripheral myelinated motor and sensory axon. These computational platforms make it possible to systematically study downstream mechanisms of peripheral nerve diseases, which cannot be assessed with experimental studies. Obtaining insight into these mechanisms is essential, because it may provide knowledge on what morphological or functional elements are most likely targeted, which aids the development of novel treatment strategies to prevent irreversible nerve damage.

Keywords: mathematical model, peripheral myelinated axon, sensory axon motor axon, neuropathies

1. Introduction

Human myelinated nerves in arms and legs have their primary function in transferring nerve impulses to mediate muscle movement or skin sensation. Immune-mediated neuropathies, such as Guillain–Barré syndrome (GBS), multifocal motor neuropathy (MMN) and acute motor axonal neuropathy (AMAN) are disorders where the body generates antibodies against its own nerves. As a result, they affect peripheral motor and sensory nerves, where nerve damage leads to loss of muscle power, loss of sensation, or both. Although the antibodies play a role in the initial attack against nerves, the downstream mechanism leading to the actual nerve dysfunction is not well understood. Knowledge of these mechanisms is essential for the development of treatments aimed at prevention of irreversible nerve damage.

Available methods in patients, like needle electromyography(EMG), EMG, nerve conduction studies (NCS), excitability test, single axon tracing, voltage or current clamp methods. These methods are invasive for the patient and are inaccurate, no channel disruptions or dynamics can directly be detected. These methods also take mostly a lot of time to perform(1,2). Furthermore, experimental methods in single myelinated axons are considerably more difficult to perform in mammalian and human fibers than in amphibian fibers, due to extreme fragility of the fibers and because they are surrounded by large connective tissue. Additionally, experimental findings in single myelinated amphibian or lower mammalian axons cannot always be extrapolated to human axons due to essential differences in ion-channel characteristics(3).

We developed a peripheral motor and sensory axon model with this present study and aimed to systematically study downstream mechanism, which cannot be assessed with experimental studies. For instance, about selective involvement of motor axons at the peripheral nerve level, such as in MMN and AMAN or about myelin damage that is associated with axonal conduction loss in trauma and chronic neurodegenerative diseases(4–6). With this peripheral axon simulation, patients do not have to come that often to a hospital for research purposes, clinical trials can be done more specific using outcome of the computer simulation. Computer simulations are relatively cheap and fast to perform, no additional tools are required.

2. Development of the mathematical model

2.1 General description

There are a lot of existing peripheral axon models(17–22), however, the model of McIntyre et al.(23) has also described paranodal, juxtaparanodal and internodal compartments in his model and was available in MATLAB and was easy to adjust to our needs. Therefore, we chose to extend the double cable model of McIntyre et al.(23) in this study.

The original model of McIntyre et al. (23) represents a detailed description of voltage-gated ion-channels in the node of Ranvier and simplified internodal membrane dynamics. As it does not contain internodal voltage-gated ion-channels, we extended the model by including a more detailed description of the internodal membrane dynamics and described the functional differences between peripheral

human myelinated motor and sensory axon. As starting point, we used the MATLAB implementation of this model as published by Danner et al. (24), and subsequently modified it for the specific purposes of this study (MATLAB 2016b, MathWorks). Numerical integration of the differential equations was performed with the CVODE diferential equation solver from the Suite of nonlinear differential/algebraic equation solvers (SUNDIALS, version 2.6.1)(25) with time steps of 0.001 ms. The sundialsTB MATLAB bindings, supplied with the SUNDIALS distribution were used to interface the CVODE solver in MATLAB.

For the longitudinal model we used in total 41 nodes of Ranvier separated by 40 internodes. The fiber geometry was kept as the original McIntyre et al.(23), where from node-to-node, the model consists of 11 segments geometrically representing the node(1 segment), paranode (paranodal myelin attachment, 1 segment), the juxtaparanode (paranodal main segment, 1 segment), the internode (6 segments), and again the juxtaparanode (1 segment), and paranode (1 segment). The double cable structure at the paranode juxtaparanode and internode for the myelin sheath was represented as a myelin conductance and myelin capacitance. The geometric parameters for an axon fiber diameter of 10.0, 14.0 and 16.0 µm are shown in table 1. (23)

Table 1: *The model geometric parameters for fiber diameters of 10.0, 14.0 and 16.0 µm. Each compartment consists of 2 paranodal and 2 juxtaparanodal regions and 6 standard internodal regions. All parameters, beside the number of myelin lamella, are in µm.*

	Fiber diameter		
	10.0	14.0	16.0
Node-node separation(23,33)	1150	1400	1500
Number of myelin lamella(12,23)	120	140	150
Node length(23,34,35)	1	1	1
Node diameter(23,34,35)	3.3	4.7	5.5
Paranode length(11,23)	3	3	3
Paranode diameter(11,12,23)	3.3	4.7	5.5
Paranode periaxonal space width(11,23)	0.002	0.002	0.002
Juxtaparanode length(11,23)	46	56	60
Juxtaparanode diameter(11,12,23)	6.9	10.4	12.7
Juxtaparanode periaxonal space width(11,23)	0.004	0.004	0.004
Standard internode length(23,33)	175.2	213.5	228.8
Standard internode diameter(12,23)	6.9	10.4	12.7
Standard internode periaxonal space width(11,23)	0.004	0.004	0.004

2.2 Membrane dynamics of the myelinated motor axon model

We adjusted the original model as obtained by Danner et al.(24) which is based on the model of McIntyre et al.(23) and developed a peripheral motor and sensory axon simulation.

In the original model of McIntyre et al.(23) the node of Ranvier contained a voltage-gated transient and persistent sodium channel, voltage-gated slow potassium channels, a leak conductance and a nodal membrane capacitance. The dynamics of these ion-channels were based on experimental studies of Scholz et al.(26) Schwarz et al.(27) and Reid et al.(28) To simulate a human myelinated axon model as closely as possible, McIntyre et al. modified the parameters of membrane dynamics to those assessed in human peripheral motor nerve excitability test for fiber diameters of 10.0 µm, 14.0 µm and 16.0 µm, see table 1(19,20,23). Also, the temperature-dependency, and gating kinetics were based on earlier experimental work in human myelinated axons(23,26–28) . We chose to set the resting membrane potential at -80 mV in case of simulation of a peripheral motor axon. Table 2 shows the membrane dynamics of the model.

***Table 2**: Conductance and capacitance values of each compartment. The value in bracket is the value for sensory simulations if this is chosen different from the motor axon simulations.*

Vrest(23,36)	-80 mV (-78 mV)
Axoplasmic + periaxonal resistivity(23)	70 Ohm*cm
Myelin capacitance(23,37,38)	0.1 µF/cm^2
Capacitance of the nodal membrane[23,39]	2 µF/cm^2
Capacitance of the internodal membrane(23,39)	2 µF/cm^2
Myelin conductance(23)	0.001 S/cm^2
Paranodal conductance(23)	0.001 S/cm^2
Juxtaparanodal conductance(23)	0.0001 S/cm^2
Standard internodal conductance(23)	0.0001 S/cm^2
Na/K pump(18,32)	0.1 nA

The paranode was presented as a passive contributor by a conductance in parallel a capacitance at the axolemma(23). We chose not to implement channels in the paranode and kept it as the original. McIntyre et al.(23) described fast potassium channels in the juxtaparanode but chose not to use them in their study. Danner et al.(24) implemented an optional fast potassium channel in the juxtaparanode. Because fast potassium channels are certainly present in the juxtaparanode, we chose to implement them in our simulation(3,16,23). Furthermore, we implemented a non-specific leakage current to the juxtaparanode to compensate for channel isoforms or channels we did not incorporate in our study.

The original model of McIntyre et al.(23) did not describe any internodal channels. To more accurately describe the membrane dynamics in the internode, a series of ion-channels were additionally implemented. At the internode, the density of the sodium channels has been suggested to be approximately 1/100 compared to that of nodal sodium channels(3,13). Hence, internodal transient and persistent channels were modelled by setting their conductance to 1% compared to that of the node. Based on Waxman et al.(16) also fast and slow potassium channels are present in the internode. The

estimated density of fast potassium channels in the internode compared to the juxtaparanode is about 1/6. For the slow potassium channels its density has been suggested to be 1/30 compared to that of the nodal density(14,16). Furthermore, the voltage-gated inwardly rectifying currents (IR) flow through, hyperpolarization-activated cyclic nucleotide gated channels (HCN-channels), and play an important role in pace-making, determination of the resting membrane potential, determination of axonal threshold in human motor axons and are also implemented in the internode. (20,29,30). Like the non-specific leakage current in the juxtaparanode, we implemented a current that may stand for the isoforms of channels we did not incorporate in our study (like the unmodeled slow HCN isoforms) (14). Finally, a Na^+/K^+-pump is implemented in the internode. Although, the localization of the Na^+/K^+-pump is controversial, it has been suggested to have an internodal localization(3,15,31). Therefore, a localization of the Na^+/K^+-pump in the internode is chosen, with a value of 0.1 nA(18,19,32).

A schematic overview of the myelinated axon model can be seen in figure 1 and table 3 shows the conductances of all the implemented channels in the model.

***Table 3**: Parameter and descriptions of the conductances of all the implemented channels in the model in S/cm^2.*

Parameter	Motor	Sensory	References
Maximum nodal Na_t^+ conductance (G_{NatN})	3.0	3.0	(16,23,26,27)
Maximum nodal Na_p^+ conductance (G_{NapN})	0.010	0.010	(23,47)
Maximum nodal K_s^+ conductance (G_{KsN})	0.080	0.0411	(20,23,26,27,48)
Nodal leakage conductance (G_{LkN})	0.007	0.007	(23)
Juxtaparanodal maximum K_f^+ conductance (G_{kf})	0.02	0.02	(23,48,49)
Internodal maximum Na^+ conductance	$G_{NafN}/100$	$G_{NafN}/100$	(3)
Internodal maximum K_s^+ conductance	$G_{KsN}/30$	$G_{KsN}/30$	(16,49)
Internodal maximum K_f^+ conductance	$G_{kf}/6$	$G_{kf}/6$	(16,49)
Internodal maximum HCN conductance	0.0016	0.0022	(18–20)
Internodal leakage conductance	$G_{LkN}/330$	$G_{LkN}/330$	(18,19)

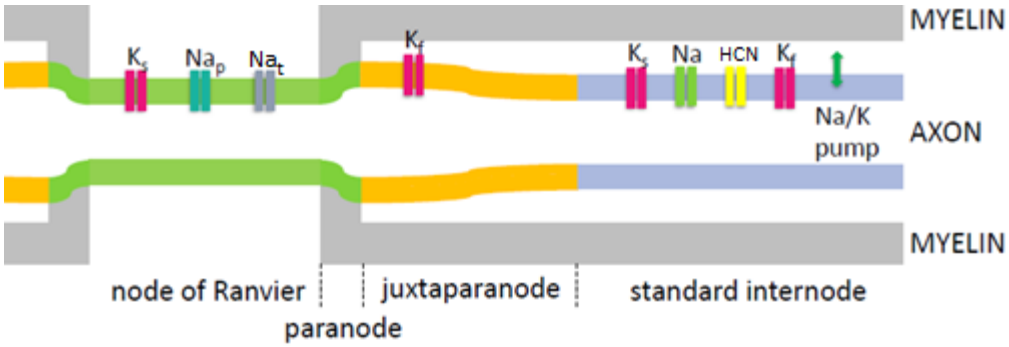

***Figure 1**: Myelinated axon diagram. Voltage-gated ion channels on the axolemma, which includes the node of Ranvier (light green), paranode(dark green), juxtaparanode(yellow), standard internode(blue). Channel descriptions; K_s: Slow potassium, Na_p: persistent sodium, Na_t: transient sodium, K_f: fast potassium, HCN: Hyperpolarization-activated cyclic nucleotide gated channels, Na/K pump: sodium/potassium pump.*

2.3 Nodal and internodal membrane dynamics of the myelinated sensory axon model

There are differences between motor and sensory axons. These are important to implement, so that a different model for sensory and motor axons can be used, to see the effects of peripheral nerve diseases, myelin damage and mechanical injuries on sensory and motor axons and for example answer questions about selective involvement of motor axons in MMN.

A prominent difference between sensory and motor axons has been suggested to be their accommodation to hyperpolarizing currents produced by HCN channels (40). The more significant accommodation to hyperpolarize currents have been ascribed to HCN channels, which are expressed more in sensory axons than in motor axons(20,31,40–43). Furthermore, increased expression of HCN channels has been suggested as a contributing factor to the greater anode break hyperexcitability seen in sensory axons(40,44). Therefore, we made adaptations to the HCN channels using the method of Howells et al. (20), combining an increase in the maximal conductance of HCN of 39% with a 13.1 mV depolarizing shift in Bq, the voltage activation of the conductance underlying HCN.

Experimental studies have shown that sensory axons are more depolarized than motor axons. Nodal and internodal slow potassium channels and the potassium equilibrium potential contribute to the resting membrane potential(14,31). Furthermore, it is hypothesized that reduces slow potassium channel expression contributed to increased susceptibility to ectopic activity in sensory axons(45,46). Adaptations to nodal slow potassium conductance is made based on the study of Howells et al. (20) and a of 49% is chosen in the sensory axon model(20). Whereas, we are using a fixed resting membrane potential in our model, adapting values of slow potassium will not eventually lead to depolarization. Therefore, the resting membrane potential of sensory axons more depolarized (-78 mV).

3. Validation of the mathematical model

3.1 Simulation protocol and validation methods

Simulations were conducted to generate the action potential, its propagation to measure the conduction velocity, the effect of temperature on conduction velocity and on the shape of the action potential, the effect of fiber diameter on the conduction velocity, and the strength-duration properties.

Single intracellular stimuli were delivered with a stimulus duration of 1 ms. The fiber diameter was set to 10.0 µm and the temperature to 36° C. To assess their effect on conduction velocity the fiber diameter was altered to 14.0 and 16.0 µm. By increasing the fiber diameter, also the axon diameter, node diameter, paranode and juxtaparanode and internode diameter increased. The length of the internode changed and the amount of lamella(myelin) surrounding the internode also increased, see table 1. The implemented temperature changes were adjusted with steps of 2 K from 299 K (26^{o}C) till 309 K(36^{o}C).

To calculate the conduction velocity, first, the derivative of the action potential was taken in every node from which the time points with maximum rising slope were determined. The internodal conduction velocity was then calculated by dividing the node-to-node distance (1150 µm, see Table 1) by the internodal conduction time. Averaging the internodal conduction velocities resulted in the overall conduction velocity of the model. To avoid boundary effects of the model the internodal conduction velocities and activation thresholds were derived from node 11 to 31.

To determine the activation threshold a binary search algorithm was applied as implemented by Hennings et al.(50) In the model, an action potential was defined as the myelinated axon was depolarized to 0 mV at the node.

From the action potential the maximum amplitude, rise time, fall time and total duration was determined. Rise and fall times were calculating by approximating the action potential as a triangle. The rise time was taken as the time from the intersection of the 10% of the difference between the resting membrane potential and the maximum amplitude till the moment of maximum amplitude. The falling time was calculated at the same manner using the falling edge (51,52).The total duration of the action potential was taken as the sum of the rise and falling times.

The strength-duration properties are characterized by the rheobase and the strength-duration time constant (SDTC)(53). SDTC is commonly assed in nerve excitability studies as a measure of axonal excitability where it depends on the biophysical properties of the axonal membrane at the node of Ranvier. It also provides information about sodium channel functioning(54). Rheobase is defined as the theoretical asymptotic current required to just excite a nerve using a stimulus with infinite duration(3). For simulating the SDTC and rheobase the changes in activation threshold was determined by varying the stimulus duration from 1 ms to 0.2 ms in steps of 0.2 ms, which is similar to that of nerve excitability testing(54).

3.2 Action potential

In figure 2 the generated action potential at the middle node of the model (node 20) for the motor (blue) and sensory (red) axon is shown after applying a 1ms intercellular stimulus pulse at node 11 with a stimulus current of 1000nA. The sensory axon starts a little bit earlier with an action potential and has a slightly lower peak amplitude(motor: 24.4 mV, sensory: 23.5 mV). Compared with the motor action potential the sensory action potential is broader. The activation threshold of node 20 is 478 nA for the motor model and 294 nA for the sensory model. Following an action potential, the models generated the characteristic depolarizing(DAP, black arrow) and hyperpolarizing afterpotentials(AHP, green arrow) (see figure 2).

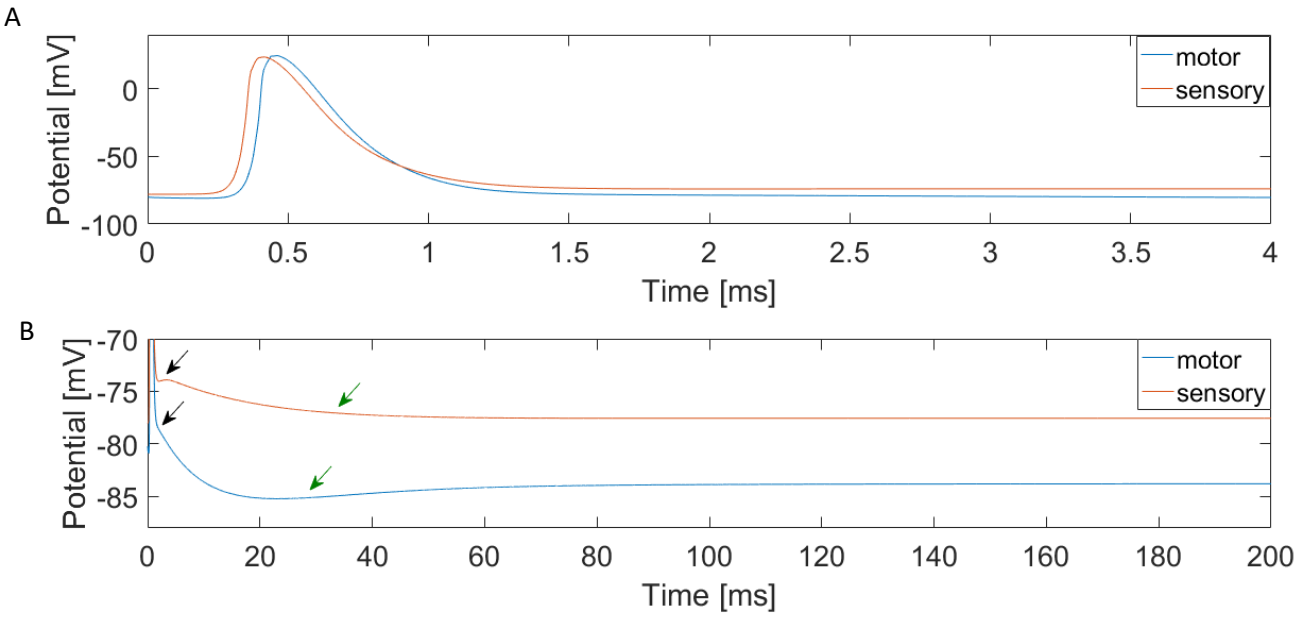

***Figure 2**: (A) The generated action potential of the motor (blue) and sensory (red) axon model up to 4ms from node 20. (B) Visualization of the same action potential as in (A), but close to its resting membrane potential(-80mV for motor and -78mV for sensory) from which the characteristic depolarizing after potential (DAP, black arrow) and hyperpolarizing afterpotential (AHP, green arrow) can be observed., for a duration of 200ms.*

3.3 Fiber diameter

The action potential propagation along nodes 11 to 31 for motor and sensory simulations can be seen in figure 3 A and B, where the line represents the steepest part from which the internodal conduction velocity was calculated, see section 3.1 for a detailed description on how the conduction velocity is calculated.

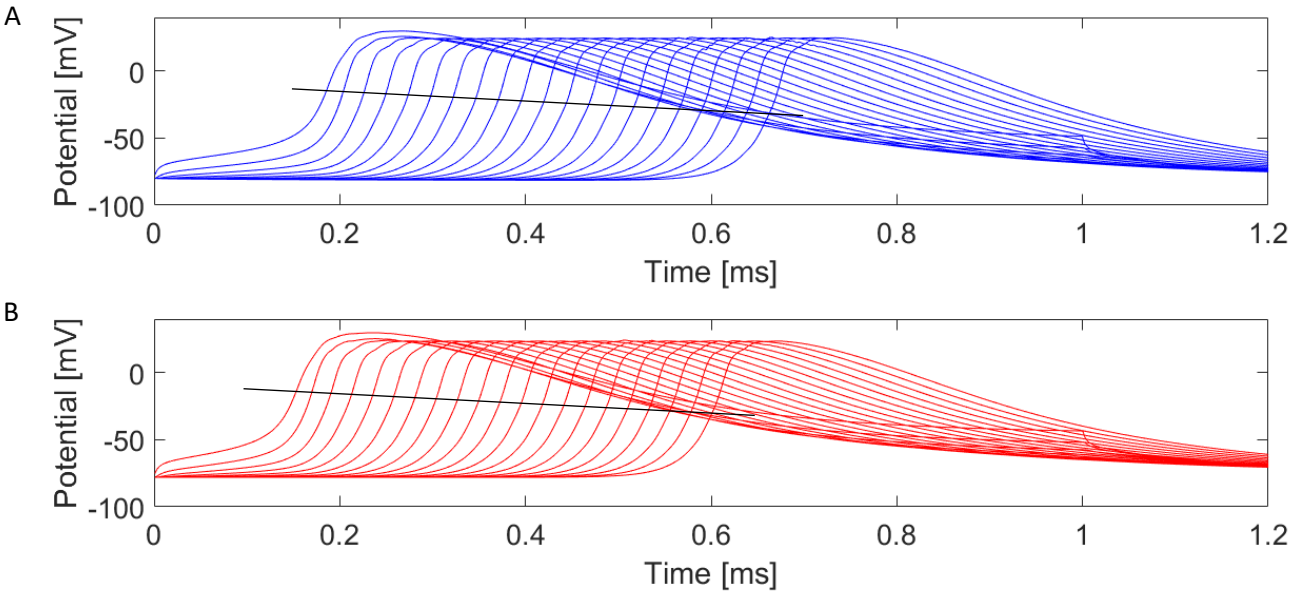

Figure 3: *Modeled action potentials at successive nodes of Ranvier(node number 11 till 31) in a model motor (A, blue) and sensory (B, red) myelinated axon. The black line represents the steepest points of the action potential*.

Changing the fiber diameter had an effect on the conduction velocity between motor and sensory axons. The conduction velocity for a fiber diameter of 10 µm was for motor and sensory axons respectively 49.9 m/sec and 53.4 m/sec. When the fiber diameter was increased to 14 µm and 16 µm the motor conduction velocity increased to respectively to 74.8 m/sec and 79.5 m/sec and the sensory conduction velocity to respectively 76.9 m/sec and 101.5 m/sec. The conduction velocity of the sensory axon is higher in respect to the conduction velocity of the motor axon and stays higher when the fiber diameter increases, see figure 4.

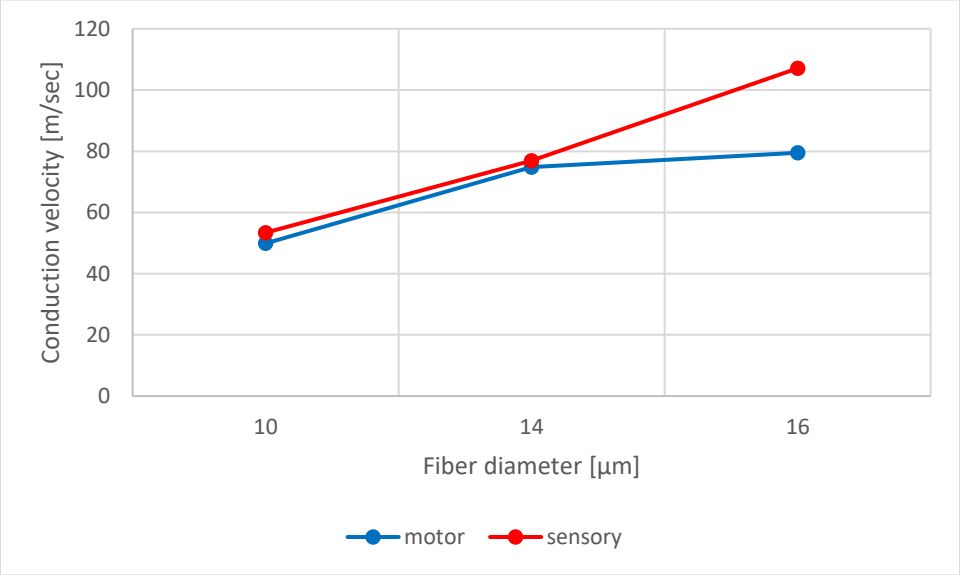

Figure 4: *Fiber diameter dependency of the conduction velocity for a motor (blue) and sensory (red) nerve fiber. The conduction velocity of the sensory axon remains higher than the motor axon and increases both when the fiber diameter increases.*

3.4 Temperature effects

In figure 5, the effect of temperature on the motor and sensory conduction velocity are shown with the expected increase in conduction velocity with increasing temperature in both the motor and sensory simulations.

The slope of the change in conduction velocity per degree in Celsius as calculated by taking a linear line from the conduction velocities 26 to 36°C and divide that with 10°C, was for the motor model 1.50 and the sensory model 1.51 m/s per °C The conduction velocity of motor axon simulations remained lower than the simulation of sensory axons. The q_{10} values as defined as a measure of the rate of change of because of the increasing temperature by 10 °C, are also different for motor and sensory simulations, which were respectively 1.44 and 1.40.

The action potential rise, fall and total times were calculated at temperatures of 26, 30 and 36°C. Figure 6 shows the definition of rise, fall and total times. Figure 7 shows the values of the rise and fall times for motor and sensory axons at different temperatures. Time rise, fall and total time decreased when the temperature increased in both motor and sensory simulations. The total action potential duration times are slightly more in sensory axon simulations in each chosen temperature, see figure 7. The maximum reached potentials of motor axons at a temperature of 26, 30 and 36°C were respectively 31.5 mV, 29.5 mV and 24.6. For sensory axons these were 30.9 mV, 28.9 mV and 23.6 mV.

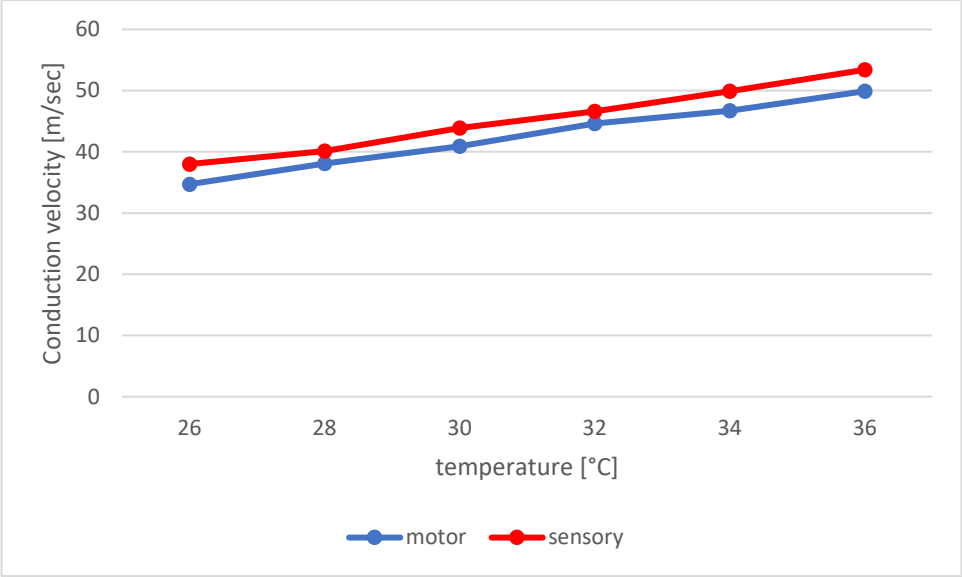

Figure 5: *Temperature dependency of conduction velocity for a motor and sensory nerve fiber. The conduction velocity of the sensory axon(red) remains higher than the motor axon(blue) and has a slightly higher slope value.*

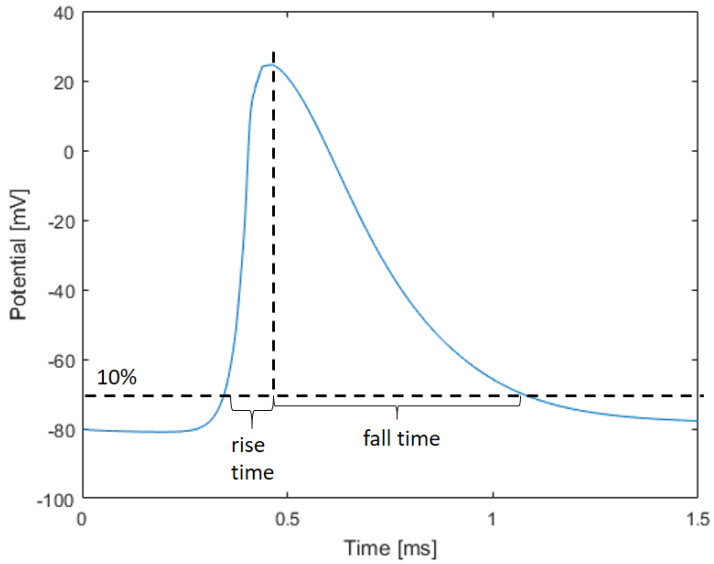

Figure 6: The description of the rise and fall time. The rise time starts at 10% of the action potential and continues till the maximum. The fall time starts at the maximum and ends at 10% of the action potential.

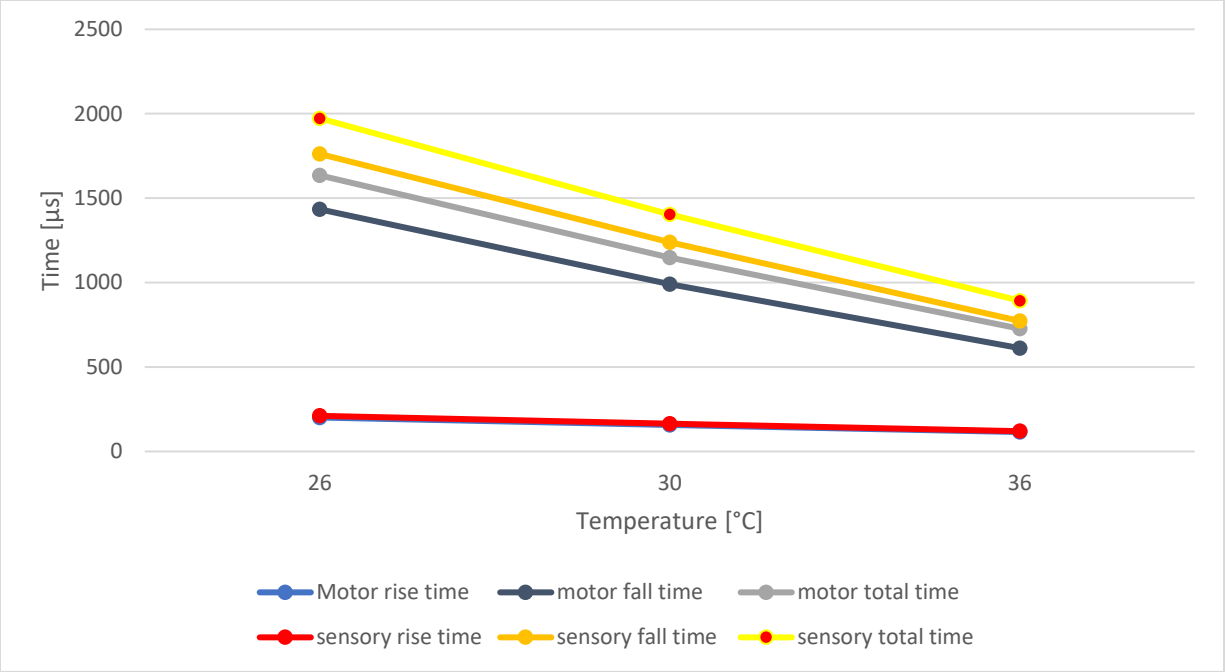

Table 7: *The rise, fall and total times of the action potentials for motor and sensory simulation at temperatures of 26°C, 30°C and 36°C. The sensory model simulation has a longer action potential duration at each chosen temperature.*

3.5 Strength-duration properties

The strength-duration properties were assessed by stimulating at node 21, using a transformation of Weiss's charge-duration equation, transformed as Bostock et al (53,56,57). Weiss proposed a linear equation using a charge Q duration curve. The electrical charge Q van be calculated with the formula:

(13) $Q = I \cdot d$ *or* $Q = b(d + SDTC)$

Where I is the current measured in amperes multiplied by the duration d. B relates to the rheobase value. Rheobase is the threshold current required if the stimulus is of infinitely long duration. In this formulation the SDTC equates to chronaxie (the stimulus duration corresponding to a threshold current that is twice rheobase). As can be seen, there is a linear relationship between charge and stimulus duration. Therefore, the rheobase and SDTC can be calculated from a charge-stimulus duration plot when different stimulus widths are used (see figure 8). The SDTC can be derived from the interception with the y-as (when the charge is 0), whereby the slope of this relationship corresponds to the rheobase.

The rheobase for the motor axon was higher with 393 pA compared to the sensory axon with 211 pA. The SDTC was lower for the motor axon with 204 µsec than the sensory axon with 385 µsec, see figure 8.

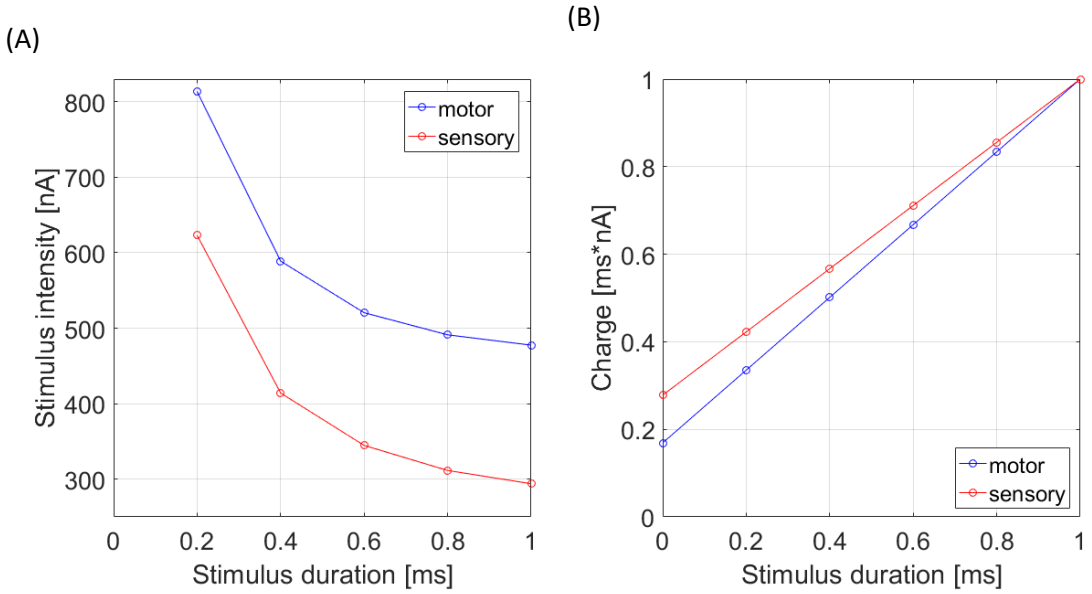

Figure 8: *(A) The strength duration curve for motor(blue) and sensory (red). The threshold value of the sensory model remains lower than the motor axon model. (B) The charge-duration curve for motor (blue) and sensory (red), the sensory charge remains larger than motor.*

In this study, we developed and validated a longitudinal peripheral myelinated motor and sensory axon model with the aim to provide a platform to systematically study downstream mechanisms in human neuropathies. The computer simulation of McIntyre et al. (23) is adapted by including internodal channels to the model. Using knowledge about differences between peripheral motor and sensory axons, differences to the motor model are made to obtain a sensory axon model. The developed model is then validated by looking at the action potential of the models, check for the channel gating kinetics and currents, look at the fiber diameter dependency of the conduction velocity and the temperature dependency of the conduction velocity and action potential rise and fall times. The last validation step was to look at the SDTC and rheobase of the two models. The model is used in a clinical application, by showing the effect of segmental demyelination (for example with MMN), on the conduction velocity in motor and sensory axons, which resulted in an earlier conduction block in motor axons (at 96% demyelination) than sensory axons (at 97% demyelination). This platform further offers the opportunity to simulate effect of drugs when targeting at specific voltage-gated ion channels.

4. Discussion

In this study, we developed and validated a longitudinal peripheral myelinated motor and sensory axon model with the aim to provide a platform to systematically study downstream mechanisms in human neuropathies. The computer simulation of McIntyre et al. (23) is adapted by including internodal channels to the model. Using knowledge about differences between peripheral motor and sensory axons, differences to the motor model are made to obtain a sensory axon model. The developed model is then validated by looking at the action potential of the models, check for the channel gating kinetics and currents, look at the fiber diameter dependency of the conduction velocity and the temperature dependency of the conduction velocity and action potential rise and fall times. The last validation step was to look at the SDTC and rheobase of the two models. This platform further offers the opportunity to simulate effect of drugs when targeting at specific voltage-gated ion channels.

4.1 Development of the model.

In this study, we simulated peripheral myelinated motor and sensory axon action potential generation and propagation by applying single intracellular stimuli. With repetitive firing during e.g. voluntary activity, additional processes can occur, such as the increase in potassium concentration in the extracellular space, especially in the periaxonal space(23,69,70). This accumulation may play an important role when the axon fires at high frequencies for an extended period, because it influences the excitability of the axon(23,71,72). Although, this cannot be captured yet with the current model, the applied stimuli protocols resemble that of standard nerve conduction studies and nerve excitability studies.

Some studies suggest that a key difference between sensory and motor axons is also the greater expression of the Na_p channel current with 200%.(2) We did not change parameters of the Na_p channel to create a greater expression of the Na channel current. In our model we accounted the depolarization change for the need for a greater expression of Na_p current(14). In our model the Na_p current change is approximately 130%. Therefore, a change in percentage Na_p is not chosen.

The ion channel types, densities, and membrane dynamics of the mammalian node of Ranvier are not completely characterized. Therefore, our model included a representation, based on available experimental data. The ion channels were modified to reproduce several different experimentally documented excitation characteristics. Some of the ion channels therefore represent a combination of channels, which match best with experimental data, like potassium channels that are normally at least five different types(23,26–28,45,48).

4.2 Validation of the model

Validation of the motor and sensory axon models gave outcome which matched with experimental studies and other mathematical simulations. The action potential showed as expected a depolarizing and hyperpolarizing after potential(73). Conduction velocities were in range with experimental studies and nerve conduction studies (NCS) (74).

Differences between motor and sensory axons are also validated. Conduction velocities of the sensory axon remained higher in sensory axon simulations than motor axon simulations. A temperature

increase, increased the conduction velocity in both motor and sensory axon, with a slightly higher slope in sensory axons as expected from previous conducted studies(44,75). The action potential was broader in sensory axons in respect to motor axons. This could be seen in the rise and fall time duration of both simulations(27,52,76,77). The broader action potential in sensory axons is earlier described and is suggested that the reduction of slow potassium channels at the node could be the reason(20). The temperature coefficient q_{10} was also within range of experimental studies(77). The conduction velocity increased with an increased axon diameter(78). Excitability studies have shown that motor axons have a smaller SDTC and larger rheobase than sensory axons(3,14,20,31,43,53,79,80). Also, a linear relationship between the charge and its duration is found as predicted by Weiss's formula(57).

4.3 Future clinical applications

Secure transmission of impulses along myelinated axons is essential for good conduction of the nerves. In various human neuropathies the clinical symptoms often indicate a prominent involvement of either motor or sensory axons. The immune-mediated neuropathy, MMN is a disorder where specifically peripheral motor nerves are affected with absence of sensory symptoms, while peripheral nerve fascicles contain both motor as well as sensory axons(1,6). The downstream mechanisms leading to the actual nerve dysfunction are not well understood and cannot be well-studied with the available experimental methods(1,2). One of the causes of conduction block in MMN is demyelination. The physiological consequences of demyelination of a single axon are slowing of the internodal conduction time, increased refractory period, persistent conduction block, rate-dependent block and warm block.(3) This can be validated after simulating demyelination. However, in the case of MMN, it remains unclear whether motor conduction block and slowing represent paranodal demyelination, segmental demyelination, changes in resting membrane potential or ion channel dysfunction at the node of Ranvier(2). To answer this question, segmental demyelination, paranodal demyelination, resting membrane deficit and an ion channel dysfunction may be implemented in the model.

Furthermore, the underlying mechanisms after mechanical injuries on peripheral nerves causing myelin disruption following axonal conduction failure could be studied and proper selection of drug treatment could be selected using treatment experiments. It is possible to simulate a mild and severe form of stretch or crush injury in the model. Using the definition of Babbs et al. (5) for a mild and severe form of stretch or crush injury. With a mild form of stretch or crush injury causing retraction of myelin around stretched nodes, which can be simulated by increasing the width of the exposed nodal membrane. A severe form of stretch or crush injury includes both retraction and detachment of paranodal myelin. Which can be simulated by decreasing paranodal resistance to one tenth or one hundredth of its normal value(5).

The mathematical model can also be used in morphological question about peripheral nerves and a broader range of immune-mediated neuropathies. It is not limited to MMN or mechanical injuries.

As a result of the mathematical model being a good representation of experimental studies, it can also be used for education purposes, to understand ion-channel dynamics, the importance of morphological aspects in conduction, and action potential propagation.

4.4 Recommendations for further development of the model

No ion channels are implemented in the myelin, despite Schwann cells express several types of ion-channels. Different types of K^+ channels, Na^+ channels, Ca^{2+} channels and ligand-gated purinergic channels. Also, Na/K pumps are expressed in the Schwann cells(81,82). These channels can be important after repetitive firing, because these channel complexes may sustain rapid repolarization after an impulse and may prevent accumulation of potassium ions. However, we only used single spikes in this study, therefore we did not expect effect of potassium accumulation in our simulations, or the need of ion-channel implementation in the myelin.

We used ion channel conductances to use the Hodgkin-Huxley equation. Some mathematical models use permeability values(17–20,22). Using permeability values, and equations gave us an unstable model, but the conductance values represented a good validation and where also earlier used by McIntyre et al. (23)

For the validation of the model, the calculation of the conduction velocity was essential. The conduction velocity is calculated by taking the time of the steepest point of each action potential. The sample frequency of the model influences the precision of the calculation of this steepest point. The time difference between each adjacent node is taken and the node to node distance is divided by the passing time. The time that passes till the steepest point is also influenced by the sample frequency. Choosing a larger sample frequency results in an action potential signal simulation which takes time (10 minutes for a simulation of 5ms, with sample frequentie of 0.001ms). However, a decrease in simulation duration can be used to decrease the calculation time.

5. Conclusion

We successfully developed a longitudinal peripheral myelinated motor and sensory axon model which matches well with experimental studies. This platform provides a place to systematically study downstream mechanisms in human neuropathies. It offers for example to study selective involvement of motor axons in MMN and AMAN or the opportunity to simulate effect of drugs when targeting at specific voltage-gated ion channels. With this platform a direction can be given to clinical research and it can be performed more effectively.